# Modelling the elastic stiffness of nanocomposites using the Mori-Tanaka method

Tom Thorvaldsen

**FFI** Forsvarets forskningsinstitutt

# Modelling the elastic stiffness of nanocomposites using the Mori-Tanaka method

Tom Thorvaldsen

Norwegian Defence Research Establishment (FFI)

19 June 2015

## Keywords

Nanoteknologi

Elastisitet

Matematiske modeller

Partikler


## Approved by

| | |
|---|---|
| Rune Lausund | Project Manager |
| Jon E. Skjervold | Director |

# English summary

This report describes mathematical modelling of the elastic stiffness of *nanocomposites*, which in this context is referred to as particles of nano-size included in a polymer matrix, i.e. particles with one dimension of nanometre size. The main motivation for this work was to establish mathematical models for calculating the elastic properties of different nanocomposites, which then can be included in a "model toolbox" for future applications and for improved understanding of this type of materials. In this study, it is assumed that micromechanics models and continuum mechanics theory can be applied in modelling.

In this report, the Mori-Tanaka method is considered, where the particles are described as having a spheroidal shape. From this assumption, the Eshelby tensor can be applied to calculate the influence of the particles to the matrix, and the overall elastic stiffness of the composite due to the inclusions. The particle shape and orientation will affect the macroscopic elastic stiffness of the composite. Thus, different spheroidal shapes (e.g. spheres, prolate and oblate) are considered, as well as both aligned and random particle orientation. The current study is, however, restricted to two-phase composites, i.e. composites with one particle inclusion phase.

When searching the literature, different models based on the Mori-Tanaka method are found. Expressions are available for specific geometric shapes and particle orientations. A more general multi-phase Mori-Tanaka model, which is applicable to several shapes and different orientations, is also found. The different models are implemented in Matlab, and the calculated model results are compared. Furthermore, the general Mori-Tanaka model is compared with experimental data found in the literature for some relevant nanoparticle/epoxy systems.

The model calculations agree very well. Moreover, the model results for the general two-phase Mori-Tanaka model agree with most of the experimental results, but the model is not able to predict the improved stiffness for low volume fractions very well. Additional studies should therefore consider other effects that will influence the elastic stiffness of the nanocomposites. First of all, more than one inclusion phase, e.g. voids, agglomerates or other particles, should be included as part of the model toolbox. Second, it is relevant to establish models that consider the effect the nanoparticle interphase, which may be modelled as a region surrounding the particles with different elastic properties compared to the neat matrix.

## Sammendrag

Denne rapporten beskriver matematisk modellering av elastisk stivhet for nanokompositter, som i denne konteksten refererer til partikler av nanostørrelse som er inkludert i en polymermatrise, det vil si partikler der en av dimensjonene er i nanometer. Hovedmotivasjonen for dette arbeidet har vært å etablere matematiske modeller som kan benyttes for å beregne de elastiske egenskapene til ulike nanokompositter, som deretter kan inkluderes i en "modellverktøykasse" for fremtidige applikasjoner og for økt forståelse av denne typen materialer. Det er antatt at mikromekaniske modeller og kontinuummekanikk kan benyttes i modelleringen.

Denne rapporten tar for seg Mori-Tanaka-metoden, der partiklene antas å ha en sfæroidal (kuleformet) fasong. Basert på denne antakelsen, kan Eshelby-tensoren benyttes for å beregne partiklenes påvirkning på matrisen, og de elastiske egenskapene til et kompositt med inklusjoner. Partiklenes fasong og orientering vil påvirke den makroskopiske elastiske stivheten til komposittet. Ulike fasonger (sfærer, fiberformede, tynne disker og nåleformede) er inkludert i studien, og videre ensrettede og tilfeldig orienterte partikler. Studien er begrenset til kompositter med én type inklusjoner, det vil si to-fase-kompositter.

Ulike modeller for nanokompositter, basert på Mori-Tanaka-metoder, er gitt i litteraturen. Uttrykk er tilgjengelig for partikler med gitte fasonger og orientering. En mer generell multi-fase Mori-Tanaka-modell, som er anvendbar for ulike fasonger og orienteringer, er også tilgjengelig. De ulike modellene er implementert i Matlab, og de beregnede modellverdiene er sammenliknet. Videre er den mer generelle Mori-Tanaka-modellen sammenliknet med eksperimentelle data for noen relevante nanopartikkel/epoksy-systemer.

Det godt samsvar mellom modellresultatene. Videre er beregningene med bruk av den generelle to-fase Mori-Tanaka-modellen i godt samsvar med de fleste eksperimentelle data. Denne modellen klarer derimot ikke å beregne stivhetsøkningen for lave volumfraksjoner veldig godt. Videre studier bør derfor vurdere andre effekter som vil påvirke stivheten til nanokomposittet. For det første bør det tas høyde for flere inklusjonsfaser, være seg hulrom, agglomerater eller andre partikler. Dessuten er det også relevant å etablere modeller som inkluderer en interfase, som kan modelleres som en region som omslutter partiklene, og som har andre elastiske egenskaper enn matrisen.

# Contents

# 1  Introduction

This report describes mathematical modelling of the elastic stiffness of *nanocomposites*, which in this context is referred to particles of nano-size included in a polymer matrix, i.e. particles with one dimension of nanometre size. The main motivation for this work is to establish a mathematical model "toolbox" for nanocomposites that can be used in future applications and for improving the understanding of this type of materials.

When establishing models for nanocomposites, several factors need to be considered. First of all, the nanomodified polymer in many cases contains very small *weight fractions*, or volume fractions[1], of nanoparticles, i.e. in the range of 1-5 wt% or less. Studies indicate that a peak weight fraction is reached for small concentrations, and that the composite properties are in fact reduced for higher concentrations; see for example [1] for the variation in conductivity. The small volume fraction  is different from, for instance, short-fibre composites, where the volume fraction is typically around 50 to 60 per cent [2]. One reason for the peak weight fraction may be that the nanoparticles introduce a very high *interfacial area*. Due to the small-sized particles, the interfacial area is much larger than what is obtained by adding larger particles [3]. Also note that the *aspect ratio* of the particles, i.e. the particle length divided by the diameter, is an important factor for defining the interfacial area. Another key factor is the *degree of dispersion* and the amount of *agglomerations*. For obtaining a good *load transfer* between the nanoparticles and the surrounding matrix, the particles should ideally be fully dispersed. Agglomerates and interacting nanoparticles will work as defects in the material instead of reinforcement. As a consequence of this, the *interphase effects*, i.e. the mechanical properties of the region surrounding the particle, as well as the *interface effects*, i.e. the load transfer at the surface between the particle and the matrix on molecular level, are also of high importance. For polymer composites containing small particles,  i.e. of nanosize, including the interphase/interface effects are said to be a requirement when doing modelling [4;5].

For particles where one dimension is larger than the other two, such as carbon nanotubes (CNTs), carbon nanofibres (CNFs) and other fibre-like nanoparticles, the particle *length distribution* and the particle *orientation distribution* are essential parameters that will influence the load transfer. As for short-fibre composites, the fibre-like nanoparticles must have a critical length to be able to transfer load. Fibre-like particles having a shorter length than the critical one will not transfer any load. The fibre orientation distribution will also affect the overall load transfer of the nanocomposite. As an example, polymer composites with aligned fibres (that are perfectly distributed and with optimal load transfer) will have higher elastic stiffness in the direction of the (stiffer) fibres, compared to the transverse direction. A composite with 3D random orientation of the fibres will macroscopically have equal properties in all directions.  The difference in composite modulus between perfectly aligned and randomly distributed fibres is estimated to be a factor of five [3]. In addition, the fibre/CNT *waviness* will influence the mechanical

---

[1] The conversion between weight fraction and volume fractions may be expressed as $W_f = (\rho_f / \rho_c)V_f$ where $W_f$ is the weight fraction of the particles, $V_f$ is the volume fraction of the particles, and $\rho_f$ and $\rho_c$ is the density of the particles and the composite, respectively.

improvement. A straight fibre/CNT is found to transfer more load than a curved fibre/CNT, see e.g. [5] and the references therein.

In the literature, two main approaches are presented for establishing mathematical models for nanocomposites [5], as illustrated in Figure 1.1. The first approach, referred to as the "bottom-up" approach, starts with quantum and molecular mechanics. From this, models for nanocomposites are established by moving to a higher scale. The second approach, referred to as the "top-down" approach, starts with models from micromechanics, laminate theory and continuum mechanics. Models for nanocomposites are then established by moving to a lower scale. Because the interaction between the nanoparticles and the surrounding matrix is on a molecular level, there is an on-going discussion on the validity of using the "top-down" approach for describing nanocomposites.

In the work presented here and the models referred to, we assume that the "top-down" approach is valid for describing nanocomposites. Furthermore, due to a variety of factors that may influence the macroscopic properties of the nanocomposite, we need to make some assumptions and simplifications to reduce the number of factors. In this work, we only consider the geometry (i.e. different ellipsoidal shapes) and orientation of the particles in the matrix (i.e. aligned and random orientation). We assume that all fibre-like inclusions are straight, and that there is full load transfer between the particles and the matrix (i.e. in the interphase). Moreover, interphase effects are neglected, the particles are perfectly dispersed in the matrix, and there are no voids in the matrix. As a consequence of this latter assumption, the study is restricted to two-phase composites.

Earlier work by the author considered short-fibre models for modelling the elastic stiffness of nanocomposites [6;7], where the same assumptions and simplifications where taken, as listed in the previous paragraph. In this report, the model toolbox for nanocomposites is extended with models based on the well-known *Mori-Tanaka method*, where the particles are assumed to have a *spheroidal shape*. This method is applicable to inclusions of different geometric shapes and sizes. The Mori-Tanaka method builds on the work by Eshelby (see Section 2), using the so-called *Eshelby tensor*. This will be briefly described before moving to the Mori-Tanaka method itself. In addition, several works report good agreement between the Mori-Tanaka model predictions and experimental results, see [5] and the references therein. In this report, different models, for both randomly distributed and aligned particles of ellipsoidal shape are presented and implemented, and the model results compared with available and relevant experimental data. Since the same assumptions are made for the short-fibre models and the Mori-Tanaka models, comparison of model results is also possible. For all cases presented in this report, the included materials for each phase of the nanocomposite are assumed to be *linearly elastic* and *isotropic*.

One or more of the assumptions and simplifications made in the study presented in this report, may give results which are neither physically representative for the composite nor in accordance with experimental data. As an extension of the current work, follow-up studies have been performed and reported: 1) three-phase models where an additional  phase is included, being

voids or agglomerates in the matrix [8], and 2) the effect of the nanoparticle interphase on the macroscopic elastic stiffness of the composite [9]. The reader is referred to the FFI reports for more details.
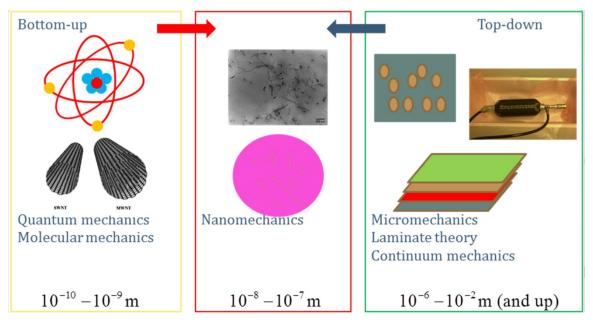


*Figure 1.1    The bottom-up versus the top-down approach for modeling of nanocomposites.*

## 2    Eshelby tensor

Eshelby derived expressions for the effect on the strain due to a spheroidal inclusion in a continuous medium [10;11]. The tensor taking into account this influence has been denoted the *Eshelby tensor*. In this report, only a brief description is provided, since the main focus is on the Mori-Tanaka method. A more detailed description of the Eshelby tensor may also be found in [12].

In the derivation of the Eshelby tensor, it is assumed that we have a homogenous linear elastic solid with volume $v$ and surface area $S$, with an *inclusion* volume $v_0$ and a surface area $S_0$, as shown in Figure 2.1.[2] The volume $v$ outside the inclusion is called the matrix.

Removing the inclusion volume $v_0$ from the surrounding matrix, the inclusion volume should assume a uniform strain. This strain is referred to as the eigenstrain, whereas the corresponding stress is referred to as the eigenstress. The eigenstress is related to the eigenstrain through Hooke's law for linear elastic materials. Note that both the matrix and the inclusion have the same elastic constants/properties in this case.

---

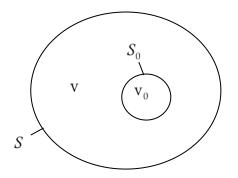[2] The volume is denoted by lowercase v to avoid confusion with the volume fraction in later sections of this report.

*Figure 2.1    A linear elastic solid with volume* $\mathrm{v}$ *and surface S. A sub volume* $\mathrm{v}_0$ *with surface* $S_0$ *undergoes a permanent (inelastic) deformation. The material inside* $\mathrm{v}_0$ *is called an inclusion, and the material outside is called the matrix.*

The Eshelby tensor $S_{ijkl}$ expresses the constrained strain inside the inclusion $e_{ij}^c$ to its eigenstrains $e_{kl}^*$,

$$e_{ij}^c = S_{ijkl}e_{kl}^* \tag{2.1}$$

Since this tensor relates two strain tensors, the Eshelby tensor satisfies the *minor symmetry* condition, i.e.

$$S_{ijkl} = S_{jikl} = S_{ijlk} \tag{2.2}$$

The Eshelby tensor, however, does not satisfy the major symmetry condition, i.e. $S_{ijkl} \neq S_{klij}$ (as do for example the fourth-order elasticity tensor for linear elastic materials [2]).

For spheroidal inclusions, the volume $\mathrm{v}_0$ occupied by the inclusion can generally be expressed as

$$\left(\frac{x'}{a}\right)^2 + \left(\frac{y'}{b}\right)^2 + \left(\frac{z'}{c}\right)^2 \leq 1 \tag{2.3}$$

where $a$, $b$ and $c$ specify the size of the spheroid, along the axis $x'$, $y'$ and $z'$, respectively. Depending on the size, we get different expressions for the Eshelby tensor. Some common shapes and corresponding tensors are given next.

The Eshelby tensor for *spherical inclusions* ( $a = b = c$ ) can be written with a compact expression,

$$S_{ijkl} = \frac{5\nu_0 - 1}{15(1 - \nu_0)} \delta_{ij}\delta_{kl} + \frac{4 - 5\nu_0}{15(1 - \nu_0)}(\delta_{ik}\delta_{jl} + \delta_{il}\delta_{jk}) \tag{2.4}$$

where $\delta_{ij}$ is the Kronecker delta, and $\nu_0$ is the Poisson's ratio of the continuous matrix. Written out for the (non-zero) coefficients, we get [13;14]

$$S_{1111} = S_{2222} = S_{3333} = \frac{7 - 5\nu_0}{15(1 - \nu_0)}$$

$$S_{1122} = S_{1133} = S_{2211} = S_{2233} = S_{3311} = S_{3322} = \frac{5\nu_0 - 1}{15(1 - \nu_0)} \tag{2.5}$$

$$S_{1212} = S_{2323} = S_{3131} = \frac{4 - 5\nu_0}{15(1 - \nu_0)}$$

Moreover, for *fibre-like spheroidal inclusions* the Eshelby tensor can be expressed as follows [13],

$$S_{1111} = \frac{1}{2(1 - \nu_0)}\left\{ 1 - 2\nu_0 + \frac{3\alpha^2 - 1}{\alpha^2 - 1} - \left[ 1 - 2\nu_0 + \frac{3\alpha^2}{\alpha^2 - 1}\right]g \right\}$$

$$S_{2222} = S_{3333} = \frac{3}{8(1 - \nu_0)}\frac{\alpha^2}{\alpha^2 - 1} + \frac{1}{4(1 - \nu_0)}\left[ 1 - 2\nu_0 + \frac{9}{4(\alpha^2 - 1)}\right]g$$

$$S_{2233} = S_{3322} = \frac{1}{4(1 - \nu_0)}\left\{ \frac{\alpha^2}{2(\alpha^2 - 1)} - \left[ 1 - 2\nu_0 + \frac{3}{4(\alpha^2 - 1)}\right]g \right\}$$

$$S_{2211} = S_{3311} = -\frac{1}{2(1 - \nu_0)}\frac{\alpha^2}{\alpha^2 - 1} + \frac{1}{4(1 - \nu_0)}\left\{ \frac{3\alpha^2}{\alpha^2 - 1} - (1 - 2\nu_0)\right\}g \tag{2.6}$$

$$S_{1122} = S_{1133} = -\frac{1}{2(1 - \nu_0)}\left[ 1 - 2\nu_0 + \frac{1}{\alpha^2 - 1}\right] + \frac{1}{2(1 - \nu_0)}\left[ 1 - 2\nu_0 + \frac{3}{2(\alpha^2 - 1)}\right]g$$

$$S_{2323} = S_{3232} = \frac{1}{4(1 - \nu_0)}\left\{ \frac{\alpha^2}{2(\alpha^2 - 1)} + \left[ 1 - 2\nu_0 - \frac{3}{4(\alpha^2 - 1)}\right]g \right\}$$

$$S_{1212} = S_{1313} = \frac{1}{4(1 - \nu_0)}\left\{ 1 - 2\nu_0 - \frac{\alpha^2 + 1}{\alpha^2 - 1} - \frac{1}{2}\left[ 1 - 2\nu_0 - \frac{3(\alpha^2 + 1)}{\alpha^2 - 1}\right]g \right\}$$

where

$$g = \frac{\alpha}{(\alpha^2 - 1)^{3/2}}\left\{ \alpha(\alpha^2 - 1)^{1/2} - \cosh^{-1}\alpha \right\} \tag{2.7}$$

and $\alpha = l / d$ is the aspect ratio of the fibre length $l$ and the fibre diameter $d$. Note that the aspect ratio is applied for indicating the size of the inclusion in this case. The aspect ratio is explicitly included in several models for fibre-like inclusions in a matrix, see e.g. [6].

For *disc-shaped spheroidal inclusions* the Eshelby tensor is given by the same expressions as in (2.6), but with $g$ replaced by $g'$ [13;14],

$$g' = \frac{\alpha}{(1-\alpha^2)^{3/2}}\left\{\cos^{-1}\alpha - \alpha(1-\alpha^2)^{1/2}\right\}$$

(2.8)

In this case, the aspect ratio $\alpha = t / a$, where $a$ and $t$ are the major and minor axes of the inclusion, with its minor axis directed along $x'$.

Alternative expressions for disc-shaped, penny-shaped, spheroidal inclusions, where $a = b \neq c$, the Eshelby tensor can be expressed as follows [12]

$$S_{1111} = S_{2222} = \frac{\pi(13-8\nu_0)}{32(1-\nu_0)}\frac{c}{a}$$

$$S_{3333} = 1 - \frac{\pi(1-2\nu_0)}{4(1-\nu_0)}\frac{c}{a}$$

$$S_{1122} = S_{2211} = \frac{\pi(8\nu_0-1)}{32(1-\nu_0)}\frac{c}{a}$$

$$S_{1133} = S_{2233} = \frac{\pi(2\nu_0-1)}{8(1-\nu_0)}\frac{c}{a}$$

$$S_{3311} = S_{3322} = \frac{\nu_0}{(1-\nu_0)}\left(1 - \frac{\pi(4\nu_0+1)}{8\nu_0}\frac{c}{a}\right)$$

$$S_{1212} = \frac{\pi(7-8\nu_0)}{32(1-\nu_0)}\frac{c}{a}$$

$$S_{3131} = S_{2323} = \frac{1}{2}\left(1 + \frac{\pi(\nu_0-2)}{4(1-\nu_0)}\frac{c}{a}\right)$$

(2.9)

Furthermore, in case of an *elliptic cylinder*, i.e. $c \rightarrow \infty$, the Eshelby tensor can be expressed as follows [12]:

$$S_{1111} = \frac{1}{2(1-\nu_0)} \left[ \frac{b^2 + 2ab}{(a+b)^2} + (1-2\nu_0)\frac{b}{a+b} \right]$$

$$S_{2222} = \frac{1}{2(1-\nu_0)} \left[ \frac{a^2 + 2ab}{(a+b)^2} + (1-2\nu_0)\frac{a}{a+b} \right]$$

$$S_{3333} = 0$$

$$S_{1122} = \frac{1}{2(1-\nu_0)} \left[ \frac{b^2}{(a+b)^2} - (1-2\nu_0)\frac{b}{a+b} \right]$$

$$S_{2233} = \frac{1}{2(1-\nu_0)} \frac{2\nu_0 a}{a+b}$$

$$S_{2211} = \frac{1}{2(1-\nu_0)} \left[ \frac{a^2}{(a+b)^2} - (1-2\nu_0)\frac{a}{a+b} \right] \tag{2.10}$$

$$S_{3311} = S_{3322} = 0$$

$$S_{1212} = \frac{1}{2(1-\nu_0)} \left[ \frac{a^2 + b^2}{2(a+b)^2} + \frac{1-2\nu_0}{2} \right]$$

$$S_{1133} = \frac{1}{2(1-\nu_0)} \frac{2\nu_0 b}{a+b}$$

$$S_{2323} = \frac{a}{2(a+b)}$$

$$S_{3131} = \frac{b}{2(a+b)}$$

Other expressions for the above mentioned shapes, as well as other shapes, may be found in the literature.

# 3  General derivation of the Mori-Tanaka method for ellipsoidal inclusions

In this section, a general derivation of the Mori-Tanaka method is presented. Since this results in fourth-order tensors that need to be truncated, an alternative formulation is derived using a vector-matrix notation, which reduces the overall dimension of the problem. The application of vector-matrix notation is possible due to the symmetry properties of the involved quantities.

## 3.1  Tensor notation

The original paper by Mori and Tanaka, describing their method, is from 1973 [15]. However, in the derivation of the Mori-Tanaka method presented in this report, we follow the derivation by Fisher and Brinson [5].

In the Mori-Tanaka method, it is assumed that the composite is comprised of $N$ phases. Phase 0 is the matrix, and the remaining $N-1$ phases are inclusion phases. The matrix phase has

stiffness $C_0$ and a volume fraction $V_0$, whereas the $r$ th inclusion phase has a stiffness $C_r$ and a volume fraction $V_r$. The quantities $C_0$ and $C_r$ are generally fourth-order elasticity tensors, with certain symmetry properties. The elasticity tensors satisfy the minor symmetry condition, i.e. $C_{ijkl} = C_{jikl} = C_{ijlk}$, which was also the case for the Eshelby tensor described in Section 2. In addition, the elasticity tensor will satisfy the major symmetry condition, i.e. $C_{ijkl} = C_{klij}$. The volume fractions are single values, i.e. constants.
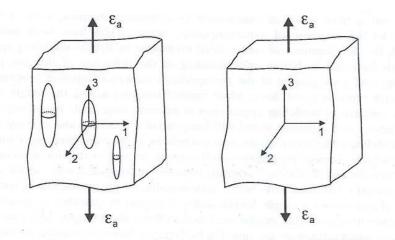


**Figure A.1.** Schematic of Mori-Tanaka method. (left) Multiphase composite material. (right) Comparison material.

*Figure 3.1 Schematic of the Mori-Tanaka method. The figure/picture is taken from [5]. Note that in this case the inclusion 3' axis is directed along the load direction. Moreover, in the current figure, a left-hand coordinate system is defined.*

Figure 3.1 shows a multi-phase composite with inclusions, as well as a comparison material. The average stress for the comparison material is given by Hooke's law,

$$\sigma_0 = C_0 \varepsilon_a \tag{3.1}$$

whereas for the composite with inclusions, the average stress is given as

$$\bar{\sigma} = C \varepsilon_a \tag{3.2}$$

Due to the inclusion, the average strain of the *matrix* of the composite will be perturbed, reading

$$\bar{\varepsilon}_0 = \varepsilon_a + \bar{\varepsilon}_0^{\mathrm{pt}} \tag{3.3}$$

where the over-score represents the volume average of the quantity, and $\bar{\varepsilon}_0^{\mathrm{pt}}$ is the perturbation strain.

The average strain of the $r$th *inclusion* is perturbed by the amount $\varepsilon_r^{\mathrm{pt}}$,

$$\bar{\varepsilon}_r = \bar{\varepsilon}_0 + \varepsilon_r^{\text{pt}} = \varepsilon_a + \bar{\varepsilon}_0^{\text{pt}} + \varepsilon_r^{\text{pt}} \tag{3.4}$$

Given that the stress in the $r$th inclusion can be given as $\bar{\sigma}_r = C_r \bar{\varepsilon}_r$, and using the equivalent method, the stress can be expressed in the terms of the matrix stiffness,

$$\bar{\sigma}_r = C_r \bar{\varepsilon}_r = C_0 (\bar{\varepsilon}_r - \varepsilon_r^*) \tag{3.5}$$

As shown in Section 2, the perturbed strain and the eigenstrain for a single ellipsoidal inclusion, can be related using the Eshelby tensor, reading

$$\varepsilon_r^{\text{pt}} = S_r \varepsilon_r^* \tag{3.6}$$

Using the above expressions, one finds that

$$\bar{\varepsilon}_r = \bar{\varepsilon}_0 + \varepsilon_r^{\text{pt}} = \bar{\varepsilon}_0 + S_r \varepsilon_r^* \tag{3.7}$$

Now, solving for $\varepsilon_r^*$ in (3.5),

$$\varepsilon_r^* = C_0^{-1}(C_0 - C_r)\bar{\varepsilon}_r \tag{3.8}$$

and inserting into (3.7),

$$\bar{\varepsilon}_r = \bar{\varepsilon}_0 + S_r C_0^{-1}(C_0 - C_r)\bar{\varepsilon}_r \Rightarrow \bar{\varepsilon}_r = A_r^{\text{dil}}\bar{\varepsilon}_0 \tag{3.9}$$

where

$$A_r^{\text{dil}} = [I + S_r C_0^{-1}(C_r - C_0)]^{-1} \tag{3.10}$$

Hence, the quantity $A_r^{\text{dil}}$ for the $r$th inclusion contains the Eshelby tensor, which depends on the shape of the inclusion, as described in Section 2.

Furthermore, it is required that the volume-weighted average phase strain must equal the far-field applied strain. From this, a strain-concentration factor can be established, that accounts for the inclusion interaction by relating the average matrix strain in the composite to the uniform applied strain. The factor reads

$$A_0 = \left[ V_0 I + \sum_{r=1}^{N-1} V_r A_r^{\text{dil}} \right]^{-1} \tag{3.11}$$

In the *r*th inclusion, the strain-concentration factor in the non-dilute composites can be written as

$$A_r = A_r^{\mathrm{dil}} A_0 \tag{3.12}$$

An effective stiffness for the composite for a *unidirectionally aligned* composite, can then be defined as

$$C_{C,alligned} = V_0 C_0 A_0 + \sum_{r=1}^{N-1} V_r C_r A_r = \left( V_0 C_0 + \sum_{r=1}^{N-1} V_r C_r A_r^{dil} \right) \left( V_0 I + \sum_{r=1}^{N-1} V_r A_r^{dil} \right)^{-1} \tag{3.13}$$

For a *randomly distributed* composite, on the other hand, averaging must be performed to take into account the orientations of the inclusions (In case of spherical inclusions, the result is the same). The stiffness matrix of the composite can now be expressed as [5],

$$C_{C,random} = \left( V_0 C_0 + \sum_{r=1}^{N-1} V_r \{ C_r A_r^{dil} \} \right) \left( V_0 I + \sum_{r=1}^{N-1} V_r \{ A_r^{dil} \} \right)^{-1} \tag{3.14}$$

where the curly brackets indicate the average of the quantity over all possible orientations.

Note that the fourth-order tensors for the matrix and the inclusions in the most general case describe anisotropic materials. In case of transverse isotropic or isotropic material properties for the constituent materials of the composite, simplifications are possible.

### 3.1.1   Orientationally-averaged fourth-order tensors

The general expression for a randomly distributed composite in (3.14) contains an orientationally-averaged fourth-order tensor that needs to be calculated.

Generally, an orientationally-averaged fourth-order tensor $\overline{B}_{ijkl}$ for a fourth-order tensor $B_{ijkl}$ in 3D space can be written as,

$$\overline{B}_{ijkl} = \{ B_{ijkl} \} = \frac{1}{2\pi} \int_0^{2\pi} \int_0^{2\pi} B_{ijkl}(\theta, \varphi) \sin \varphi \, d\varphi \, d\theta \tag{3.15}$$

In the randomization, there is a need for transforming from local to global coordinates. The transformation matrix, taking full random distribution into account, may be expressed as [14]

$$a_{ij} = \begin{bmatrix} \cos\theta & \sin\theta\cos\varphi & \sin\theta\sin\varphi \\ -\sin\theta & \cos\theta\cos\varphi & \cos\theta\sin\varphi \\ 0 & -\sin\varphi & \cos\varphi \end{bmatrix} \tag{3.16}$$

This matrix has the property $a^{-1} = a^T$, and the transformation from local to global coordinates may therefore be expressed as

$$B_{ijkl}(\theta, \varphi) = a_{ir} a_{js} a_{kt} a_{lu} B'_{rstu} \tag{3.17}$$

Now, for the $r$th inclusion, assuming that the 1' axis is the inclusion axis, i.e. directed along the inclusion, and the other two local axis lie in the 2'-3' plane and defined according to a right-hand coordinate system, we can calculate the orientationally-averaged tensor. Note that this is different from what was presented by Fisher and Brinson [5], where the 3' axis is the inclusion axis; see Figure 3.1. Using standard contraction (as applied by [16], page 65) the resulting tensor component transformations can be expressed in matrix form. For 3D random orientation of the inclusions,

$$
\begin{bmatrix}
\bar{B}_{11} \\ \bar{B}_{22} \\ \bar{B}_{33} \\ \bar{B}_{12} \\ \bar{B}_{21} \\ \bar{B}_{13} \\ \bar{B}_{31} \\ \bar{B}_{23} \\ \bar{B}_{32} \\ \bar{B}_{44} \\ \bar{B}_{55} \\ \bar{B}_{66}
\end{bmatrix}
= \frac{1}{120}
\begin{bmatrix}
24 & 64 & 0 & 16 & 16 & 0 & 0 & 0 & 0 & 0 & 0 & 64 \\
24 & 9 & 45 & 6 & 6 & 10 & 10 & 5 & 5 & 20 & 40 & 24 \\
24 & 9 & 45 & 6 & 6 & 10 & 10 & 5 & 5 & 20 & 40 & 24 \\
8 & 8 & 0 & 12 & 32 & 20 & 0 & 40 & 0 & 0 & 0 & -32 \\
8 & 8 & 0 & 32 & 12 & 0 & 20 & 0 & 40 & 0 & 0 & -32 \\
8 & 8 & 0 & 12 & 32 & 20 & 0 & 40 & 0 & 0 & 0 & -32 \\
8 & 8 & 0 & 32 & 12 & 0 & 20 & 0 & 40 & 0 & 0 & -32 \\
8 & 3 & 15 & 2 & 2 & 30 & 30 & 15 & 15 & -20 & -40 & 8 \\
8 & 3 & 15 & 2 & 2 & 30 & 30 & 15 & 15 & -20 & -40 & 8 \\
8 & 3 & 15 & 2 & 2 & -10 & -10 & -5 & -5 & 20 & 40 & 8 \\
8 & 8 & 0 & -8 & -8 & 0 & 0 & 0 & 0 & 40 & 20 & 28 \\
8 & 8 & 0 & -8 & -8 & 0 & 0 & 0 & 0 & 40 & 20 & 28
\end{bmatrix}
\begin{bmatrix}
B_{11} \\ B_{22} \\ B_{33} \\ B_{12} \\ B_{21} \\ B_{13} \\ B_{31} \\ B_{23} \\ B_{32} \\ B_{44} \\ B_{55} \\ B_{66}
\end{bmatrix}
\tag{3.18}
$$

This latter expression is then used for the averaged quantity indicated by the curly brackets (3.14). Note that a similar expression for the case where the local 3' axis is directed along the inclusion axis, may be established [5].

## 3.2 Vector-matrix notation

Since the expressions in Section 3.1 include handling of fourth-order tensors, it will be advantageous to reduce the size of the involved quantities for implementation and calculations. Considering the involved quantities, the stress and strain second-order tensors are symmetric. Moreover, the fourth-order tensors have at least minor symmetry properties (e.g. the Eshelby tensor), or both minor and major symmetry properties (e.g. the elasticity tensors for the matrix and the inclusions).

First, writing out the expression in (3.6) for the Eshelby tensor, and applying the symmetry properties of the strain tensors and the Eshelby tensor, we find that

$$
\begin{pmatrix} \varepsilon_{11}^c \\ \varepsilon_{22}^c \\ \varepsilon_{33}^c \\ \varepsilon_{12}^c \\ \varepsilon_{23}^c \\ \varepsilon_{31}^c \end{pmatrix} = \begin{pmatrix} S_{1111} & S_{1122} & S_{1133} & 2S_{1112} & 2S_{1123} & 2S_{1131} \\ S_{2211} & S_{2222} & S_{2233} & 2S_{2212} & 2S_{2223} & 2S_{2231} \\ S_{3311} & S_{3322} & S_{3333} & 2S_{3312} & 2S_{3323} & 2S_{3331} \\ S_{1211} & S_{1222} & S_{1233} & 2S_{1212} & 2S_{1223} & 2S_{1231} \\ S_{2311} & S_{2322} & S_{2333} & 2S_{2312} & 2S_{2323} & 2S_{2331} \\ S_{3111} & S_{3122} & S_{3133} & 2S_{3112} & 2S_{3123} & 2S_{3131} \end{pmatrix} \begin{pmatrix} \varepsilon_{11}^* \\ \varepsilon_{22}^* \\ \varepsilon_{33}^* \\ \varepsilon_{12}^* \\ \varepsilon_{23}^* \\ \varepsilon_{31}^* \end{pmatrix} \tag{3.19}
$$

Using *engineering shear strains* in the above relation, we obtain the expression

$$
\begin{pmatrix} \varepsilon_{11}^c \\ \varepsilon_{22}^c \\ \varepsilon_{33}^c \\ \gamma_{12}^c \\ \gamma_{23}^c \\ \gamma_{31}^c \end{pmatrix} = \begin{pmatrix} S_{1111} & S_{1122} & S_{1133} & S_{1112} & S_{1123} & S_{1131} \\ S_{2211} & S_{2222} & S_{2233} & S_{2212} & S_{2223} & S_{2231} \\ S_{3311} & S_{3322} & S_{3333} & S_{3312} & S_{3323} & S_{3331} \\ 2S_{1211} & 2S_{1222} & 2S_{1233} & 2S_{1212} & 2S_{1223} & 2S_{1231} \\ 2S_{2311} & 2S_{2322} & 2S_{2333} & 2S_{2312} & 2S_{2323} & 2S_{2331} \\ 2S_{3111} & 2S_{3122} & 2S_{3133} & 2S_{3112} & 2S_{3123} & 2S_{3131} \end{pmatrix} \begin{pmatrix} \varepsilon_{11}^* \\ \varepsilon_{22}^* \\ \varepsilon_{33}^* \\ \gamma_{12}^* \\ \gamma_{23}^* \\ \gamma_{31}^* \end{pmatrix} \tag{3.20}
$$

The coefficients of the Eshelby tensor in the two latter expressions are dependent on the geometry of the inclusion, as shown in Section 2.

In a similar way, the general Hooke's law for linear elastic solids can be expressed [2],

$$
\begin{pmatrix} \sigma_{11} \\ \sigma_{22} \\ \sigma_{33} \\ \sigma_{12} \\ \sigma_{23} \\ \sigma_{31} \end{pmatrix} = \begin{pmatrix} E_{1111} & E_{1122} & E_{1133} & 0 & 0 & 0 \\ E_{1122} & E_{2222} & E_{2233} & 0 & 0 & 0 \\ E_{1133} & E_{2233} & E_{3333} & 0 & 0 & 0 \\ 0 & 0 & 0 & E_{1212} & 0 & 0 \\ 0 & 0 & 0 & 0 & E_{2323} & 0 \\ 0 & 0 & 0 & 0 & 0 & E_{3131} \end{pmatrix} \begin{pmatrix} \varepsilon_{11} \\ \varepsilon_{22} \\ \varepsilon_{33} \\ \gamma_{12} \\ \gamma_{23} \\ \gamma_{31} \end{pmatrix} \tag{3.21}
$$

Note that the engineering shear strains have been applied also in the latter expression.

The above relations are now employed in expressions similar to the final expressions in Section 3.1 for aligned and randomly oriented ellipsoidal inclusions, (3.13) and (3.14), respectively. These expressions are relatively easy to implement in a computer program, such as Matlab.

# 4 Specialized expression for the elastic stiffness of nanocomposites

The general derivation of the multi-phase Mori-Tanaka model in Section 3 considered composites with $N-1$ inclusion phases. However, for most nanocomposites the matrix contains only one or two types of particle inclusions. Several papers therefore present more specialized analytical expressions based on for the Mori-Tanaka method for the elastic stiffness of nanocomposites. These expressions are then established for specific nanocomposites, containing inclusions with isotropic or anisotropic material properties, with a specific geometric shape, and with either aligned or random orientations. The simplest case is spherical isotropic inclusions, for which we do not have to take into account the direction dependency of the inclusions; composites with unidirectionally aligned and randomly distributed spherical isotropic inclusions have the same elastic properties. Composites with spherical inclusions having anisotropic material properties, or other (spheroidal) shapes, require more complex expressions that must take into account the orientation dependency.

Examples of more specialized expressions for nanocomposites will be presented in the following subsections.

## 4.1 Spherical inclusions

### 4.1.1 Spheres with isotropic material properties

Weng [17] presented a model for a two-phase composite, i.e. with one type of spherical isotropic inclusions. The normalized properties of the composite are given by the composite bulk modulus $\kappa_{comp}$ and shear modulus $\mu_{comp}$,

$$\frac{\kappa_{comp}}{\kappa_0} = 1 + \frac{V_1}{\dfrac{3c_0\kappa_0}{3\kappa_0 + 4\mu_0} + \dfrac{\kappa_0}{\kappa_1 - \kappa_0}}$$

$$\frac{\mu_{comp}}{\mu_0} = 1 + \frac{c_1}{\dfrac{6}{5}\dfrac{c_0(\kappa_0 + 2\mu_0)}{3\kappa_0 + 4\mu_0} + \dfrac{\mu_0}{\mu_1 - \mu_0}} \qquad (4.1)$$

where the material properties of the constituents are calculated from the isotropic bulk and shear moduli of the matrix (phase 0) and the inclusion (phase 1). Moreover, following their notation, $c_0$ and $c_1$ are the volume fraction of the matrix and inclusion phase, respectively, with $c_0 + c_1 = 1$.

From the above expressions, the longitudinal Young's modulus, normalized by the Young's modulus of the matrix can be written,

$$\frac{E_{comp}}{E_0} = \frac{\kappa_{comp}\mu_{comp}(3\kappa_0 + \mu_0)}{3\kappa_{comp}\kappa_0 + \mu_{comp}\mu_0} \qquad (4.2)$$

In a similar way, a three-phase composite can be expressed, where the bulk moduli, shear moduli and the volume fractions of the three constituent materials are included. Details are found in the referred paper; the model is also described in [8].

### 4.1.2 Spheres with anisotropic material properties

Qiu and Weng [18] presented a more general model for spherical inclusions that also include spherical inclusions with anisotropic material properties. An orientational averaging then needs to be included. Their expressions yield

$$
\kappa = \left( \frac{c_0}{\kappa_0^* + \kappa_0} + \frac{c_1}{\kappa_0^* + \kappa_1 - a_1^2 / (\mu_0^* + \mu_1)} \right)^{-1} - \kappa_0^*
$$

$$
\mu = \left[ \frac{c_0}{\mu_0^* + \mu_0} + \frac{c_1}{5} \left( \frac{1}{\mu_0^* + \mu_1 - a_1^2 / (\kappa_0^* + \kappa_1)} + \frac{2}{\mu_0^* + m_1} + \frac{2}{\mu_0^* + p_1} \right) \right]^{-1} - \mu_0^*
$$

(4.3)

where

$$
\kappa_0^* = \frac{4}{3} \mu_0
$$

$$
\mu_0^* = \frac{\mu_0}{6} \left( \frac{9\kappa_0 + 8\mu_0}{\kappa_0 + 2\mu_0} \right)
$$

$$
\kappa_1 = \frac{1}{9} (4k_1 + 4l_1 + n_1)
$$

(4.4)

$$
\mu_1 = \frac{1}{3} (k_1 - 2l_1 + n_1)
$$

$$
a_1^2 = (n_1 + l_1 - 2k_1)^2 / 27
$$

with $k_1$ being the plane-strain bulk modulus, $l_1$ the cross modulus, $n_1$ the axial modulus under an axial strain, and $m_1$ and $p_1$ are the transverse and axial shear moduli, respectively. Phase 0 is the matrix, and phase 1 is the inclusion. Moreover, $c_0$ and $c_1$ are the volume fraction of the matrix and inclusion phase, respectively.

In the case of isotropic material properties for phase 1, $k_1 = \kappa_1 + 1/3 \, \mu_1$, $l_1 = \kappa_1 - 2/3 \, \mu_1$, $n_1 = \kappa_1 + 4/3 \, \mu_1$, and $m_1 = p_1 = \mu_1$. In this case, $\kappa_1$ and $\mu_1$ are the bulk and shear moduli, and the parameter $a_1$, i.e. the so-called "anisotropic factor", vanishes.

## 4.2 Unidirectionally aligned spheroidal inclusions

### 4.2.1 Tandon and Weng model

Tandon and Weng [13] presented a model for the elastic moduli of a composite with unidirectionally aligned isotropic spheroidal inclusions, covering prolate (i.e. fibre-like) and

oblate (i.e.disc-like) inclusions, as well as spherical inclusions. The general constants applied in the derivations are given by

$$A_1 = D_1(B_4 + B_5) - 2B_2$$
$$A_2 = (1 + D_1)B_2 - (B_4 + B_5)$$
$$A = 2B_2B_3 - B_1(B_4 + B_5)$$
$$B_1 = V_f D_1 + D_2 + (1 - V_f)(D_1 S_{1111} + 2S_{2211})$$
$$B_2 = V_f + D_3 + (1 - V_f)(D_1 S_{1122} + S_{2222} + S_{2233})$$
$$B_3 = V_f + D_3 + (1 - V_f)[S_{1111} + (1 + D_1)S_{2211}]$$
$$B_4 = V_f D_1 + D_2 + (1 - V_f)(S_{1122} + D_1 S_{2222} + S_{2233})$$
$$B_5 = V_f + D_3 + (1 - V_f)(S_{1122} + S_{2222} + D_1 S_{2233})$$
$$D_1 = 1 + \frac{2(\mu_1 - \mu_0)}{(\lambda_1 - \lambda_0)}$$
$$D_2 = \frac{(\lambda_0 + 2\mu_0)}{(\lambda_1 - \lambda_0)}$$
$$D_3 = \frac{\lambda_0}{(\lambda_1 - \lambda_0)}$$

(4.5)

In the above expressions, $\lambda_q$ and $\mu_q$ ($q = 0, 1$) are the Lamé constants of the matrix (phase 0) and inclusions (phase 1), respectively, which in terms of the Young's modulus and Poisson's ratio can be expressed as,

$$\lambda_q = \frac{E_q \nu_q}{(1 + \nu_q)(1 - 2\nu_q)}$$
$$\mu_q = \frac{E_q}{2(1 + \nu_q)}$$

(4.6)

Finally, $V_f$ is now the volume fraction of the inclusion, and $S_{ijkl}$ is the Eshelby tensor.

From the above expressions, the longitudinal Young's modulus, normalized by the Young's modulus of the matrix, can be written,

$$\frac{E_{comp,11}}{E_0} = \frac{A}{A + V_f(A_1 + 2\nu_0 A_2)}$$

(4.7)

### 4.3 Randomly oriented spheroidal inclusions

#### 4.3.1 Tandon and Weng model

Tandon and Weng [14] presented an analytical model for the effective moduli of a 3D randomly oriented nanocomposite. This is in fact the only analytical model based on the Mori-Tanaka method the author has found for randomly oriented spheroidal inclusions applicable to fibre-like inclusions; the model includes all types of spheroidal inclusions with an aspect ratio $\alpha$.

The matrix and the inclusions have linear isotropic material properties. Expressions for the effective bulk modulus and the effective shear modulus are established. These moduli are then applied for calculating the effective Young's modulus of the composite.

The effective bulk and shear moduli of the composite are in this case given by

$$\frac{\kappa_{comp}}{\kappa_0} = \frac{1}{1+cp} \tag{4.8}$$

and

$$\frac{\mu_{comp}}{\mu_0} = \frac{1}{1+cq} \tag{4.9}$$

respectively, where $c$ is the volume fraction of the inclusions, and with $p = p_2 / p_1$, and $q = q_2 / q_1$, where

$$\begin{aligned}
p_1 &= 1 + c[2(S_{1122} + S_{2222} + S_{2233} - 1)(a_3 + a_4) + (S_{1111} + 2S_{2211} - 1)(a_1 - 2a_2)] / 3a \\
p_2 &= [a_1 - 2(a_2 - a_3 - a_4)] / 3a \\
q_1 &= 1 - c\Big\{ \frac{2}{5} \frac{2S_{1212} - 1}{2S_{1212} + \mu_0 / (\mu_1 - \mu_0)} + \frac{1}{3} \frac{2S_{2323} - 1}{2S_{2323} + \mu_0 / (\mu_1 - \mu_0)} - \frac{1}{15a} \\
&\quad \times [(S_{1122} - S_{2233})(2a_3 - a_4 + a_5 a) + 2(S_{1111} - S_{2211} - 1)(a_1 + a_2) + \\
&\quad (S_{1122} - S_{2222} + 1)(2a_3 - a_4 - a_5 a)] \Big\} \\
q_2 &= -\frac{2}{5} \frac{1}{2S_{1212} + \mu_0 / (\mu_1 - \mu_0)} - \frac{1}{3} \frac{1}{2S_{2323} + \mu_0 / (\mu_1 - \mu_0)} + \frac{1}{15a} \\
&\quad \times [2(a_1 + a_2 - a_3) + a_4 + a_5 a]
\end{aligned} \tag{4.10}$$

The constants $a_i$ ($i = 1, 2, 3, 4, 5$) and $a$ in the above expressions are functions of the material properties of the constituent materials and the Eshelby tensor.

From the above quantities, the normalized Young's modulus for the composite can be expressed as

$$\frac{E_{comp}}{E_0} = \frac{\kappa_{comp}\mu_{comp}(3\kappa_0 + \mu_0)}{3\kappa_{comp}\kappa_0 + \mu_{comp}\mu_0}$$

(4.11)

Unfortunately, the expression for the constant $a$ is not completely written out in the paper. The model is therefore not directly accessible for implementation and for comparison with the other modeling approaches.

### 4.3.2  Qiu and Weng model

Qiu and Weng [18] presented models for randomly oriented needles (or circular fibres) and randomly oriented thin discs, in addition to the model for spherical inclusions with anisotropic material properties, as described in Section 4.1.2.

In case of *randomly oriented needle inclusions*,

$$\kappa_{comp} = \kappa_V - c_1 \left[ 1 - c_1 \frac{2k_1 + l_1 - 3\kappa_0}{3(k_1 + \mu_0)} \right]^{-1} \left[ \frac{(2k_1 + l_1 - 3\kappa_0)(2k_1 + l_1 - 3\kappa_V)}{9(k_1 + \mu_0)} \right]$$

$$\mu_{comp} = \mu_V - \frac{c_1}{5} \left[ 1 - c_1 \frac{k_1 - l_1 - \mu_0}{15(k_1 + \mu_0)} - \frac{2}{5}c_1 \frac{m_1 - \mu_0}{m_1 + \gamma_0} - \frac{2}{5}c_1 \frac{p_1 - \mu_0}{p_1 + \mu_0} \right]^{-1}$$

$$\cdot \left[ \frac{(k_1 - l_1 - \mu_0)(k_1 - l_1 - \mu_V)}{3(k_1 + \mu_0)} + \frac{2(m_1 - \mu_0)(m_1 - \mu_V)}{m_1 + \gamma_0} + \frac{2(p_1 - \mu_0)(p_1 - \mu_V)}{p_1 + \mu_0} \right]$$

(4.12)

where the Voigt bounds $\kappa_V$ and $\mu_V$ are given by

$$\kappa_V = c_0\kappa_0 + c_1\kappa_1$$

$$\mu_V = c_0\mu_0 + \frac{c_1}{5}(\mu_1 + 2m_1 + 2p_1)$$

(4.13)

with

$$\gamma_0 = \mu_0 \left( \kappa_0 + \frac{1}{3}\mu_0 \right) / \left( \kappa_0 + \frac{7}{3}\mu_0 \right)$$

(4.14)

In the case of isotropic material properties for the inclusions, $m_1 = p_1 = \mu_1$.

For *randomly oriented discs* the expressions yield

$$\kappa_{comp} = \kappa_V - c_1 \left[ 1 - c_1 \frac{2l_1 + n_1 - 3\kappa_0}{3n_1} \right]^{-1} \left[ \frac{(n_1 + 2l_1 - 3\kappa_0)(n_1 + 2l_1 - 3\kappa_V)}{9n_1} \right]$$

$$\mu_{comp} = \mu_V - \frac{c_1}{5} \left[ 1 - \frac{2}{15}c_1 \frac{n_1 - l_1 - 2\mu_0}{n_1} - \frac{2}{5}c_1 \frac{p_1 - \mu_0}{p_1} \right]^{-1}$$

$$\cdot \left[ \frac{(n_1 - l_1 - 2\mu_0)(n_1 - l_1 - 2\mu_V)}{3n_1} + \frac{2(p_1 - \mu_0)(p_1 - \mu_V)}{p_1} \right]$$

(4.15)

where the Voigt bounds are given in (4.13).

In both cases, the Young's modulus can be expressed as

$$\frac{E_{comp}}{E_0} = \frac{\kappa_{comp}\mu_{comp}(3\kappa_0 + \mu_0)}{3\kappa_{comp}\kappa_0 + \mu_{comp}\mu_0}$$

(4.16)

The parameters in the above expressions are the same as for the model described in Section 4.1.2.

# 5    Nanoparticle/epoxy composite systems

Different nanoparticle/polymer systems are presented in the literature. In this report, a set of five relevant systems are considered in the analysis. In all cases, the epoxy and the inclusion materials have isotropic properties.

The material properties for the first two composite systems considered are given in Table 5.1 and Table 5.2 for a glass/epoxy composite [14] and a graphite/epoxy composite [18], respectively. The epoxies are a bit different for these two composite systems. However, the graphite inclusion has a much higher Young's modulus compared to glass, effects of which can be seen in the composite elastic stiffness comparison.

*Table 5.1    Material data for glass/epoxy nanocomposites, with elastic properties from [14].*

| Material parameter | Unit | Value |
|---|---|---|
| *Matrix:* | | |
| Young's modulus | GPa | 2.76 |
| Poission's ratio | | 0.35 |
| *Glass inclusion:* | | |
| Young's modulus | GPa | 72.4 |
| Poisson's ratio | | 0.20 |

*Table 5.2    Material data for graphite/epoxy nanocomposites, with elastic properties from [18].*

| Material parameter | Unit | Value |
|---|---|---|
| *Matrix:* | | |
| Young's modulus | GPa | 3.50 |
| Poission's ratio | | 0.42 |
| *Graphene inclusion:* | | |
| Young's modulus | GPa | 226.93 |
| Poission's ratio | | 0.30 |

For the three following systems, experimental data are also available for comparing with the models results. Different surface treatments and accelerators are applied for the systems involved. This requires detailed knowledge of material chemistry, which is outside the scope of the current study. Thus, in this report only the elastic parameters are applied in the models, without focusing on the test specimen preparation.

Johnsen *et al.* [19] have presented results from preparation and characterization of nanoalumina/epoxy composites. The elastic properties in this case are given in Table 5.3. Two different nanoparticles were considered in the work: 1) spherical particles, and 2) whiskers (i.e. fibre-like) particles. The alumina particles have a higher stiffness than graphite, which makes this system relevant to compare with the two first systems.

*Table 5.3    Material data for alumina/epoxy nanocomposites, with elastic properties from [19].*

| Material parameter | Unit | Value |
|---|---|---|
| *Matrix:* | | |
| Young's modulus | GPa | 3.12 |
| Poission's ratio | | 0.35 |
| *Alumina inclusion:* | | |
| Young's modulus | GPa | 386 |
| Poission's ratio | | 0.22 |

Johnsen *et al.* [20] have also presented results from preparation and characterization of nanosilica/epoxy composites. The silica particles are spherical. Johnsen *et al.* report a very good dispersion of the particles – at least for the low particle concentrations. The elastic properties in this case are given in Table 5.4; the Poisson's ratio of the silica particles is not given by Johnsen *et al.*, and is thus set to 0.20.

*Table 5.4    Material properties for nanosilica/epoxy composites, with elastic properties from [20].*

| Material parameter | Unit | Value |
|---|---|---|
| *Matrix:* | | |
| Young's modulus | GPa | 2.96 |
| Poisson's ratio | | 0.35 |
| *Silica inclusion:* | | |
| Young's modulus | GPa | 70 |
| Poisson's ratio | | 0.20 |

Graphene oxide (GO) has also been considered as a relevant filler material in nanocomposites, see e.g. Gudarzi and Sharif [21] . Material values for a composite with functionalized graphene oxide (fGO) in an epoxy matrix are given in Table 5.5.  Since Gudarzi and Sharif compare their experimental results with the Halpin-Tsai model, no Poisson's ratio is given. For simplicity, the same Poisson's ratio value is applied for both the fGO and epoxy in the current calculations, where the value is based on a typical value found for carbon nanotubes (CNTs).

*Table 5.5    Material data for fGO/epoxy composites [21].*

| Material parameter | Unit | Value |
|---|---|---|
| *Matrix:* | | |
| Young's modulus | GPa | 2.80 |
| Poisson's ratio | | 0.35 |
| *fGO inclusion:* | | |
| Young's modulus | GPa | 250 |
| Poisson's ratio | | 0.35 |

# 6    Comparison of model results

The purpose of the current section is to verify the code implementation and to compare the model results obtained from using the general multi-phase Mori-Tanaka model in Section 3 with the calculations from employing the specialized expressions in Section 4.  Some experiences with the model implementation are also included.

Three of the material systems in Section 5 are included in the results summary presented in this section, that is the glass/epoxy composite (Table 5.1), the graphite/epoxy (Table 5.2) and the alumina/epoxy (Table 5.3) composite systems. In the next section (see Section 7), some of the model results will also be compared to experimental data.

The models have been implemented in the commercial software package Matlab. The complete code in each case is given in Appendix B.
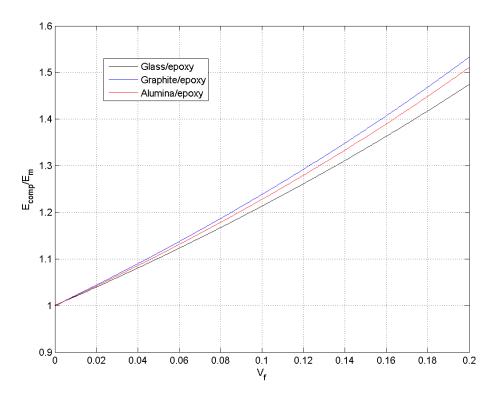
## 6.1 Spherical inclusions

The models for composites with isotropic spherical inclusions included in this study, are compared, and the calculated elastic stiffness, as a function of the volume fraction of the inclusions, is found to agree and be the same for all models.

The isotropic spherical particles are independent of orientation. For verification of the code implementation, the implemented models for randomly oriented spherical particles, with isotropic material properties, are also run. These model results also agree with the model results for aligned spherical inclusions, as expected.
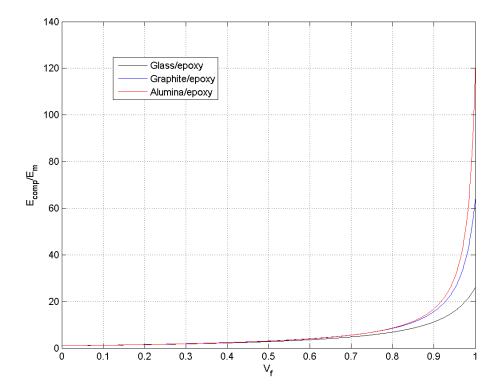
When applying the general multi-phase Mori-Tanaka model (in Section 3), no orientational averaging of the quantities in the second factor of (3.14) is performed. Otherwise the same elastic stiffness is not obtained for the case of randomly orientation spheres and aligned spheres. This deviates from the stiffness expression for random oriented inclusions, where an averaging is performed. Why an orientation averaging of the second factor of (3.14) affects the elastic stiffness for composites spherical isotropic inclusions is not clear. It might be that the averaging operation matrix is not applicable for spherical particles, or that the case of spherical particles is not covered by this particular model; enough details are not provided by Fisher and Brinson [5]. It should also be mentioned that the elastic stiffness for the composite with spherical randomly oriented (isotropic) particles deviates significantly from the stiffness calculated by the model for the composite with aligned spherical (isotropic) inclusions for high volume fractions, i.e. for volume fractions higher than 0.2. High volume fractions are, however, not relevant for this type of composite.

Figure 6.1 shows the normalized Young's modulus for the composite as a function of volume fraction of the inclusion material for three of the composite material systems considered. For low concentrations, the stiffness increase is slightly different for the three systems, and is dominated by the elastic stiffness of the polymer matrix. The graphite/epoxy composite is thus the composite with the largest stiffness increase. The glass/epoxy composite results in the lowest stiffness increase, and the alumina/epoxy composite is somewhere in-between. A larger difference in the elastic stiffness increase is observed for higher volume fractions, see Figure 6.2, where the stiffness properties of the inclusion become the more dominant material. The alumina/epoxy composite then becomes the composite with the highest elastic stiffness. The results are as expected.

As a separate case, the spherical inclusion phase in the three matrix systems is assumed to have zero stiffness, i.e. simulating voids in the matrix. Figure 6.3 shows this case. Since the three epoxy systems have close to the same elastic stiffness, the values are very similar, and hence only one curve is shown in the plot. As expected, there is a reduction in the stiffness of the matrix due to the void content, and the stiffness is dramatically reduced for higher void fractions.

*Figure 6.1    Spherical inclusions. Three different composite materials are considered.*



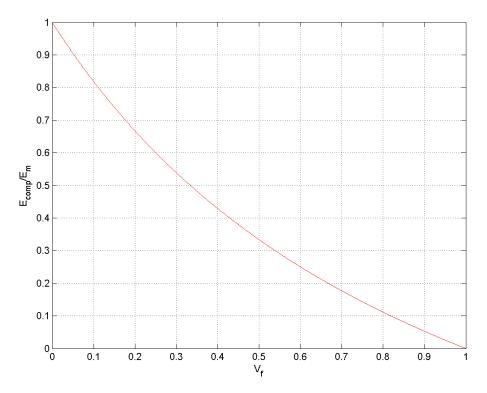*Figure 6.2    Spherical inclusions. Three different composite materials are considered.*

*Figure 6.3    Composite elastic stiffness as a function of volume fraction of voids in the matrix.*

## 6.2    Fibre-like inclusions

For nanocomposites with fibre-like inclusions, different elastic stiffness in the load direction will be obtained for the case of aligned inclusions and for the case of randomly oriented inclusions. In the case of randomly oriented fibre-like inclusions, only the general Mori-Tanaka model in Section 3 is available.

### 6.2.1    Aligned inclusions

For the case of aligned fibre-like inclusions, the aspect ratio is set to $\alpha = 20$. The composite elastic stiffness calculated from employing the two available and implemented models for aligned fibre-like inclusions agree very well.

Figure 6.4 and Figure 6.5 show the normalized composite elastic stiffness for the three material systems considered. As is observed, the stiffness properties of the inclusions dominate the stiffness of the composite for all volume fractions. This is different from the stiffness calculations for the composites with spherical particles considered in Section 6.1, where the inclusion phase dominated for very high volume fractions only. The stiffness is highest for the alumina/epoxy composite, and lowest for the glass/epoxy composite. In this case, the graphite/epoxy composite is somewhere in between. This is as expected.
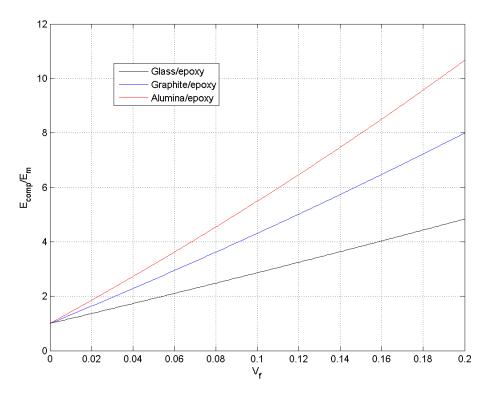
*Figure 6.4    Fibre-like aligned inclusions. Three different composites are considered.*
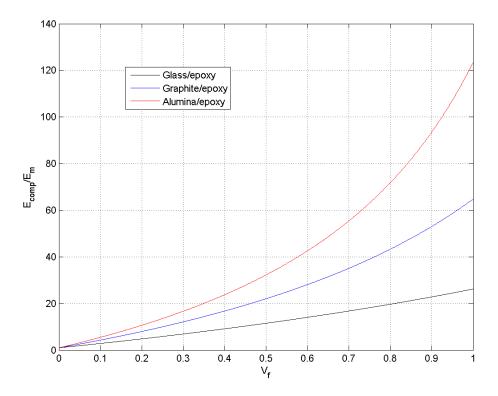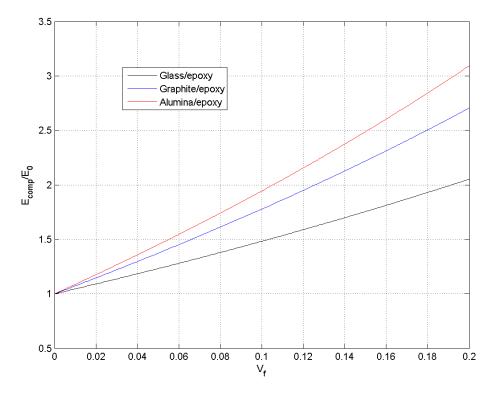


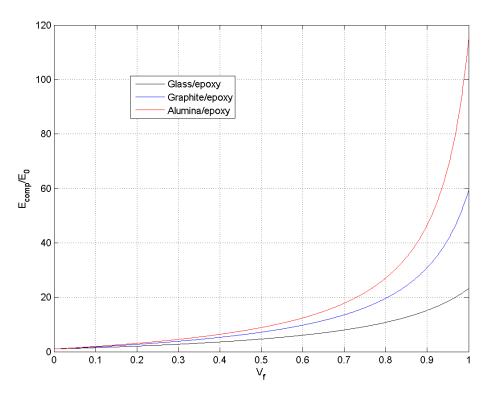*Figure 6.5    Fibre-like aligned inclusions. Three different composites are considered.*

## 6.2.2 Randomly oriented inclusions

For randomly oriented inclusions, only the general multi-phase Mori-Tanaka model is available. The three different material systems considered are included in the comparison. For the systems, the aspect ratio is set to $\alpha = 20$.

As can be seen in Figure 6.6 and Figure 6.7, the composite stiffness is dominated by the elastic stiffness of the inclusions. The highest stiffness is obtained for the alumina/epoxy composite, and the results are similar to the case of aligned fibre-like inclusions, see Section 6.2.1. Also, note that the stiffness of the composites with aligned inclusions is 2-3 times higher than for the composites with randomly oriented inclusions.



*Figure 6.6   Fibre-like randomly oriented inclusions. Three different composite materials are considered.*

*Figure 6.7 Fibre-like randomly oriented inclusions. Three different composite materials are considered.*

## 6.3 Disc shaped inclusions

### 6.3.1 Aligned

Two different models are implemented for aligned disc shaped, or oblate shaped, inclusions. The aspect ratio is set to $\alpha = 0.5$. The calculated elastic stiffness agree for the two models.

The three composite systems are included also in this case. Figure 6.8 shows the composites stiffness for low volume fractions. The matrix seems to dominate the elastic stiffness of the composite, and hence the graphite/epoxy composite has the highest stiffness increase, and the glass/epoxy composite has the lowest stiffness increase. Considering the same material systems for higher concentrations, as shown in Figure 6.9, the stiffness of the inclusions starts to dominate, and the alumina/epoxy composite then has the highest elastic stiffness value. The results are as expected.
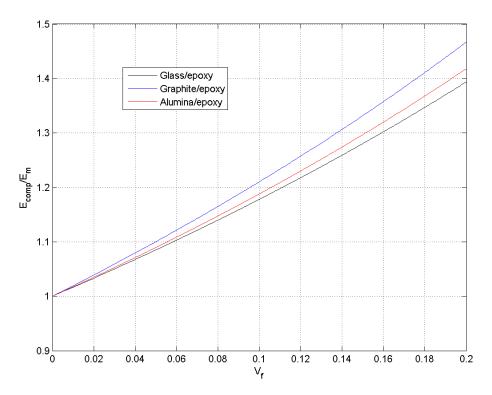
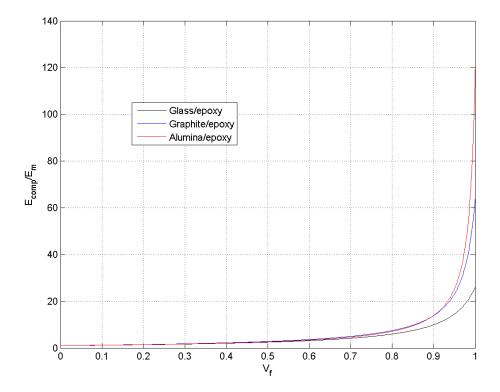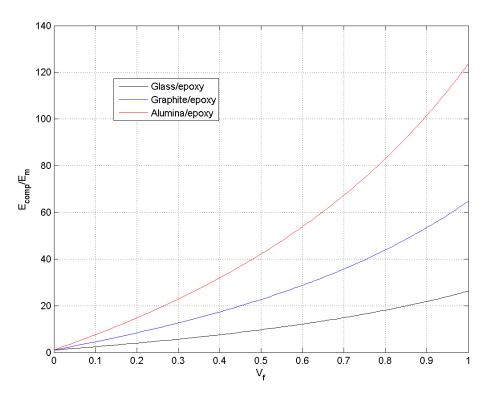*Figure 6.8   Disc shaped aligned inclusions. Three different composite materials are considered.*



*Figure 6.9   Disc shaped aligned inclusions. Three different composite materials are considered.*

## 6.3.2 Randomly oriented

Two different models are available for randomly oriented disc shaped inclusions. The models are not directly comparable, due to the fact that the Qiu and Weng model [18] does not explicitly contain the aspect ratio of the inclusions. For the general multi-phase Mori-Tanaka model, on the other hand, the aspect ratio can be set and adjusted. In this test case, the model results are therefore plotted in separate plots. It should, however, be mentioned that setting the aspect ratio to $\alpha = 0.00005$ in the general Mori-Tanaka model, i.e. very flat discs, gives the same stiffness values as obtained from the Qiu-Weng model.
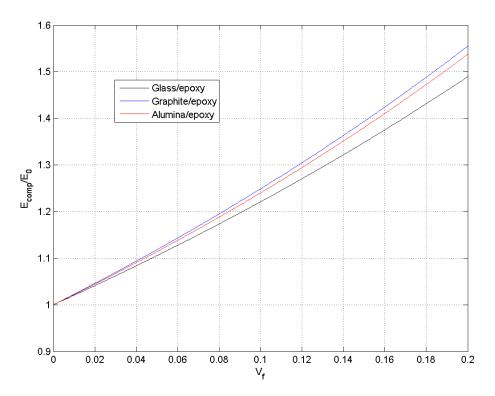
### 6.3.2.1 Qiu and Weng model

The normalized composite elastic stiffness for the three considered material systems is shown in Figure 6.10. In the same way as for randomly oriented fibre-like inclusions, the composite stiffness is dominated by the stiffness of the inclusions. As expected, the alumina/epoxy composite has the highest elastic stiffness.



*Figure 6.10 Disc shaped randomly oriented inclusions. Three different composite materials are considered.*

### 6.3.2.2 The general Mori-Tanaka model

The normalized composite stiffness using the general multi-phase Mori-Tanaka model is shown in Figure 6.11. The aspect ratio is set to 0.5. With this aspect ratio, the stiffness of the matrix dominates the composite stiffness for low volume fractions, see Figure 6.11. For higher volume fractions, see Figure 6.12, the inclusion material dominates the composite stiffness.

*Figure 6.11 Disc shaped randomly oriented inclusions. Three different composite materials are considered.*



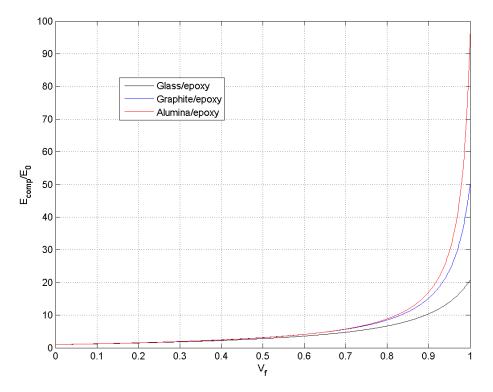*Figure 6.12 Disc shaped randomly oriented inclusions. Three different composite materials are considered.*

## 6.4    Needles

### 6.4.1    Randomly oriented

One model is available for needle shaped inclusions. The calculated composite stiffness as a function of volume fraction is shown in Figure 6.13 for the three composite material systems considered. As the fibres are very long, the inclusion stiffness dominates the composite stiffness and the alumina/epoxy composite has the highest elastic stiffness.

This case is the most relevant case for comparison with continuous fibre models. Moreover, it shows the range of possible nanocomposite materials that can be modelled using the Mori-Tanaka method.



*Figure 6.13  Needle shaped randomly oriented inclusions. Three different composite materials are considered.*

# 7    Comparison with experimental data

For some of the composite systems listed in Section 5, experimental data is available. The purpose of this section is to compare the model calculation with experimental data. As a conclusion from Section 6, the general multi-phase Mori-Tanaka model and the more specialized models give the same composite stiffness as a function of volume fraction. Therefore, in this section only the general Mori-Tanaka model has been applied in the comparison with the experimental data.

## 7.1 Alumina/epoxy composite

### 7.1.1 Spherical inclusions

Experimental data for spherical nanoalumina particles embedded in epoxy is given in Table 7.1. Two different techniques are applied for the dispersion of the particles, that is, horn sonication and bath sonication. Moreover, a silane (GPS) surface treatment is applied for improving the adhesion between the particles and the surrounding matrix. More details are found in [19]. The data set is very small, which means that it may be difficult to draw any conclusions on the agreement between the calculated elastic stiffness and the experimental values. However, improved understanding on the effect of alumina inclusions can be obtained.

*Table 7.1    Experimental results for the elastic properties of alumina/epoxy nanocomposites with spherical inclusions. The data are taken from [19].*

| Material type | Sonication | wt% | Nominal $V_f$ | Tensile modulus, E (MPa) |
|---|---|---|---|---|
| Epoxy | N/A | N/A | 0.0 | $3120 \pm 110$ |
| NT-50nm | Bath | 1.0 | 0.00350 | $3150 \pm 100$ |
| NT-50nm | Bath | 4.0 | 0.01385 | $3220 \pm 130$ |
| NT-50nm | Horn | 1.0 | 0.00345 | $3400 \pm 190$ |
| NT-50nm | Horn | 2.9 | 0.01025 | $3240 \pm\ \ 70$ |
| GPS-50nm | Bath | 3.0 | 0.01060 | $3290 \pm 130$ |
| GPS-50nm | Horn | 1.0 | 0.00345 | $3130 \pm\ \ 60$ |

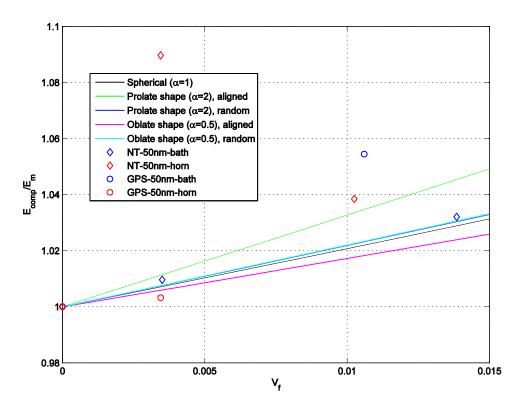(NT= Non-treated; GPS = silane treated)

*Figure 7.1    Mori-Tanaka models for spherical inclusions. Model results are compared with experimental data from Johnsen et al. [19] .*

The black curve in Figure 7.1 gives the normalized Young's modulus of the nanoalumina/epoxy composite with spherical inclusions as a function of particle volume fraction. As can be observed in the figure, there is good correspondence between the model results and the experimental data in case of employing the bath sonication procedure. For the test specimen where the horn sonication procedure has been used, and the case of using horn sonication together with particle surface treatment, the model seems to underestimate the stiffness. For specimens where the GPS treated particles  are dispersed using bath sonication, the Mori-Tanaka model overestimates the elastic stiffness of the composite.

In addition to the case of perfect spherical particles, curves are also included in the plot for cases where the particles have a slightly deformed shape. Two different shapes are included, that is 1) a prolate shape, with aspect ratio 2, and 2) an oblate shape, with aspect ratio 0.5. Both aligned and randomly distributed inclusions are considered and plotted since the orientation now will affect the stiffness in the load direction. As can be seen in Figure 7.1, the prolate and oblate random orientations result in the same stiffness increase. This is as expected, because of the choice of aspect ratios. The curves are also very close to the curve for spherical particles. The aligned prolate particle case, as shown by the green curve, gives a higher stiffness compared to spherical particles. This model prediction agrees with the experimental data for the test specimens where bath sonication is used. Finally, the aligned oblate particle case results in a lower stiffness for the composite, which seems to underestimate the stiffness values obtained in the experiments.

## 7.1.2 Fibre-like inclusions

The experimental data for alumina whisker inclusions are shown in Table 7.2. In the same way as for the spherical particles, two different sonication techniques are applied. In this case, no surface treatment is applied for improving of the adhesion between the particles and the surrounding matrix. The aspect ratio is set to 20; the value is chosen to get a best fit with the experimental data. In the same way as for the spherical alumina particles, more data is required before drawing any conclusions on the behaviour and properties of the nanocomposite.

*Table 7.2    Experimental results for the elastic properties of alumina/epoxy nanocomposites with whisker inclusions. The data are taken from [19].*

| Material type | Sonication | wt% | Nominal $V_f$ | Tensile modulus, E (MPa) |
|---|---|---|---|---|
| Epoxy | N/A | N/A | 0.0 | $3120 \pm 110$ |
| NT-whiskers | Bath | 0.1 | 0.00035 | $3310 \pm 140$ |
| NT-whiskers | Bath | 1.0 | 0.00350 | $3360 \pm 110$ |
| NT-whiskers | Bath | 3.0 | 0.01060 | $3450 \pm 170$ |
| NT-whiskers | Bath | 5.0 | 0.01730 | $3540 \pm 130$ |
| NT-whiskers | Horn | 0.1 | 0.00035 | $3210 \pm 190$ |
| NT-whiskers | Horn | 1.0 | 0.00345 | $3390 \pm 120$ |
| NT-whiskers | Horn | 2.9 | 0.01025 | $3360 \pm 140$ |

(NT = Non-treated; GPS = silane treated)

As can be observed from Figure 7.2, the calculated elastic stiffness of the nanocomposite with randomly oriented whiskers inclusions agrees very well with the experimental data. The good match for the aspect ratio of 20 is unexpected.  Information provided by the supplier, indicates an aspect ratio of around 100. The whiskers may, however, be broken during the sonication, and all whiskers may not have the same initial aspect ratio. Moreover, the assumption of perfect dispersion, optimal load transfer and a perfect random distribution may also be part of the explanation.

For comparison, the case of aligned whiskers with the same aspect ratio (i.e. $\alpha = 20$) is also plotted in Figure 7.2, see the magenta curve. This stiffness curve may be seen as an upper bound for the elastic stiffness of the nanocomposite. The model overestimates the elastic stiffness of the composite – especially for higher volume fractions.
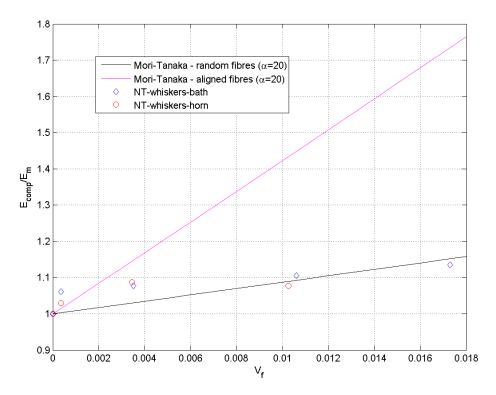
*Figure 7.2   Mori-Tanaka model for randomly oriented whiskers.  Model results are compared
with experimental data from Johnsen et al. [19] .*

### 7.1.2.1  Aspect ratio

To further investigate the mechanical properties of the alumina whiskers/epoxy composite, the
composite stiffness for different aspect ratios are calculated. Figure 7.3 and Figure 7.4 show the
results for aligned and randomly oriented whiskers, respectively. The composite elastic stiffness
increases as the aspect ratio value is increased. For aspect ratios higher than 1000, no significant
improvement of the stiffness is obtained. The cyan curve therefore indicates a practical upper
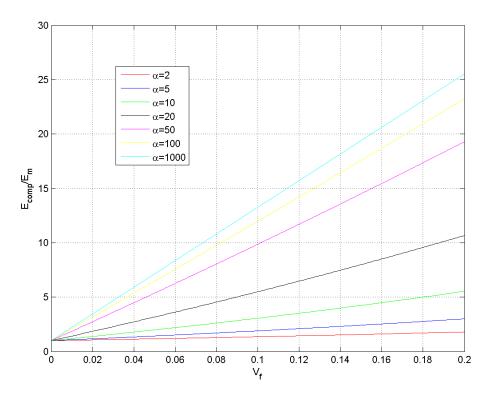limit for the elastic stiffness of the nanocomposite.
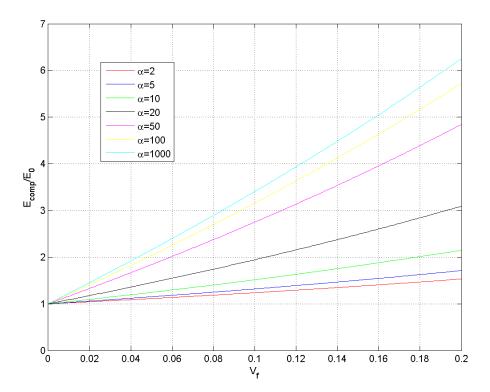
*Figure 7.3    Aligned alumina whiskers.*



*Figure 7.4    Random alumina whiskers.*

## 7.2   Silica/epoxy composites

Experimental results for the elastic stiffness of silica/epoxy nanocomposites are reported by Johnsen *et al.* [20]. The obtained elastic stiffness values for the nanocomposites with spherical nanosilica particles are given in Table 7.3.

The blue curve in Figure 7.5 shows the model results from using the general two-phase Mori-Tanaka model. As can be seen, the results agree very well for higher volume fractions. For lower volume fractions, the Mori-Tanaka model underestimates the elastic stiffness of the composite. One explanation to this may be that the interphase effects need to be taken into account, as emphasized by, e.g., Fisher and Brinson [5]. For lower volume fractions this is crucial to include in the modelling, whereas the same effect do not seem to be significant for higher volume fractions. A further study of this case is included in [9].

*Table 7.3    Experimental results for the elastic properties of silica/epoxy composites with spherical inclusions. The data are taken from [20].*

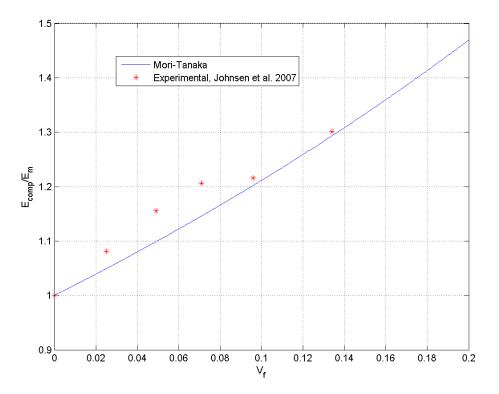| Material type | wt% | Nominal $V_f$ | Tensile modulus, E (MPa) |
|---|---|---|---|
| Epoxy | N/A | 0.0 | $2960 \pm 200$ |
| Nanosilica-epoxy | 4.1 | 0.025 | $3200 \pm 150$ |
| Nanosilica-epoxy | 7.8 | 0.049 | $3420 \pm 180$ |
| Nanosilica-epoxy | 11.1 | 0.071 | $3570 \pm 130$ |
| Nanosilica-epoxy | 14.8 | 0.096 | $3600 \pm\ \ 50$ |
| Nanosilica-epoxy | 20.2 | 0.134 | $3850 \pm 240$ |

*Figure 7.5    Silica/epoxy composite. Experimental results from Johnsen et al. [20].*

## 7.3    Graphene oxide/epoxy composites

Some experimental results for nanocomposites with amine-fuctionalized graphene oxide (fGO) particles are reported by Gudarzi and Sharif  [21]. The experimental stiffness values for different vol% of fGO particles are based on Figure 12 in [21].

Gudarzi and Sharif compares the experimental results to the Halpin-Tsai model for *aligned* short-fibre composites. In their paper, this model is referred to as a model for randomly oriented fibre-like particles. Perfect bonding is assumed between the particles and the matrix, and the applied aspect ratio of the particles is $\alpha = 350$ .

As can be seen from Figure 7.6, the experimental results agree well with the Halpin-Tsai model and the Mori-Tanaka model for *aligned* inclusions. No alignment is, however, performed in the preparation of the test specimen. Also, observe that the experimental results do not agree well with the Mori-Tanaka model for *random orientation* of the fGOs. Other effect than alignment of the particles may contribute to the stiffness improvement obtained experimentally.
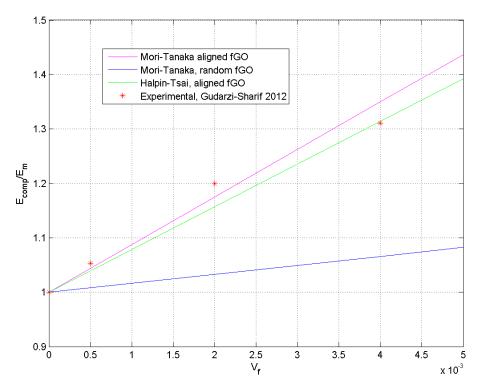
*Figure 7.6   Functionalized graphene oxide/epoxy composites. Experimental data from [21].*

# 8   Summary

In this report, several models for the elastic stiffness of nanocomposites have been described. All models are based on the method by Mori and Tanaka for spheroidal inclusions in a matrix, and the theory by Eshelby is applied for including the effect of the inclusions. The Mori-Tanaka method is applicable to particles with spheroidal shapes, including aligned and randomly oriented particles. Specialized expressions for nanocomposites with a specific inclusion geometry and orientation are also established. A more general two-phase Mori-Tanaka model is also developed. The latter model is applicable to particles of different spheroidal shape, and both aligned and randomly oriented particles. All models are implemented in the commercial software package Matlab.

The models are compared and found to agree very well for different particle shapes. Three different material systems are considered, where the stiffness properties of the constituent materials of the composite systems vary. For spherical particles, the stiffness increase for the composites is dominated by the matrix stiffness for low volume fractions and by the particle stiffness for high volume fractions. For non-spherical particles, the composite elastic stiffness is dominated by the particles for both low and high volume fractions.

The composite stiffness calculations from using the general two-phase Mori-Tanaka model are also compared with experimental data for three different nanocomposites. The model calculations are found to agree well with most of the experimental data. Including other effects in the models may, however, be required.

Future studies should include models for studying the elastic stiffness of nanocomposites with more than one inclusion phase. In case of more than one type of inclusion, the inclusion phases may, for example, be two different types of particles. Alternatively, one of the inclusion phases can be a particle, whereas the other phase is voids. A third possibility is a nanocomposite with a combination of dispersed particles and agglomerates of (the same) particles, where the particle agglomerates are treated as an inclusion material with different properties compared to the dispersed particles. Further, future research could study the influence of an interphase region surrounding the particles. The interphase elastic properties are generally higher or lower than the properties of the bulk matrix. The thickness of the interphase may also influence the elastic stiffness of the composite.

## Acknowledgements

# Appendix A     Model summary

Table A.1 and Table A.2 give the Matlab file name for each of the implemented model, as well as references to the papers and types of inclusions.

The Matlab codes for all models are given in Appendix B.

*Table A.1     Models for aligned inclusions.*

| File name | Reference | Inclusion geometry | | |
|---|---|---|---|---|
| | | **Spherical** | **Fiber-like** | **Disc shaped** |
| mori_tanaka_1.m | [13] | X | X | X |
| mori_tanaka_3.m | [5;13;14] | X | X | X |

*Table A.2     Models for randomly oriented inclusions.*

| File name | Reference | Inclusion geometry | | | | |
|---|---|---|---|---|---|---|
| | | **Spherical isotropic** | **Spherical anisotropic** | **Fiber-like** | **Disc shaped** | **Needles (circular fibres)** |
| mori_tanaka_4.m | [18] | X | X | | X | X |
| mori_tanaka_5.m | [17] | X | | | | |
| mori_tanaka_6.m | [5;13;14] (*) | X | | X | X | |
| mori_tanaka_7.m | [5;13;14] (**) | X | | X | X | |

*(\*) Local inclusion axis being the 1' axis. Eshelby tensors as in the referenced papers.*

*(\*\*) Local inclusion axis being the 3' axis. Redefined Eshelby tensors compared to referenced papers.*

# Appendix B    Matlab code

## B.1    General Mori-Tanaka model for aligned inclusions

```
% Mori-Tanaka – general model
% File name: "mori_tanaka_3.m"
% Generally: Model N-1 spheroidal shaped inclusions in an isotropic
matrix
% This case: One type of isotropic inclusion
% Three geometries:
% 1) aligned spherical inclusions
% 2) aligned fibre-like inclusions with aspect ratio
% 3) aligned disc-shaped inclusion with aspect ratio
%
% Author: Tom Thorvaldsen, FFI, March 2014

% Elastic properties - matrix
E_0 = 2.96
nu_0 = 0.35

C = zeros (6,6);
const = (E_0*(1-nu_0))/((1+nu_0)*(1-2*nu_0));
C(1,1) = const;
C(1,2)= const*(nu_0/(1-nu_0));
C(1,3)= const*(nu_0/(1-nu_0));
C(2,1) = C(1,2);
C(2,2) = const;
C(2,3) = const*(nu_0/(1-nu_0));
C(3,1) = C(1,3);
C(3,2) = C(2,3);
C(3,3) = const;
C(4,4) = const*((1-2*nu_0)/(2*(1-nu_0)));
C(5,5) = const*((1-2*nu_0)/(2*(1-nu_0)));
C(6,6) = const*((1-2*nu_0)/(2*(1-nu_0)));
C;

% Elastic properties - inclusion
E_i = 70
nu_i = 0.20

D = zeros (6,6);
const = (E_i*(1-nu_i))/((1+nu_i)*(1-2*nu_i));
D(1,1) = const;
D(1,2)= const*(nu_i/(1-nu_i));
```

```
D(1,3)= const*(nu_i/(1-nu_i));
D(2,1) = D(1,2);
D(2,2) = const;
D(2,3) = const*(nu_i/(1-nu_i));
D(3,1) = D(1,3);
D(3,2) = D(2,3);
D(3,3) = const;
D(4,4) = const*((1-2*nu_i)/(2*(1-nu_i)));
D(5,5) = const*((1-2*nu_i)/(2*(1-nu_i)));
D(6,6) = const*((1-2*nu_i)/(2*(1-nu_i)));
D;


% Geometry:
geom = 1  % spherical inclusions
%geom = 2  % fibre-like inclusions
%geom = 3  % disc shaped inclusions

if (geom == 1)
  % Spherical inclusions:
  S_1111 = (7-5*nu_0)/(15*(1-nu_0));
  S_2222 = S_1111
  S_3333 = S_1111
  S_1122 = (5*nu_0-1)/(15*(1-nu_0));
  S_1133 = S_1122
  S_2211 = S_1122
  S_2233 = S_1122
  S_3311 = S_1122
  S_3322 = S_1122
  S_1212 = (4-5*nu_0)/(15*(1-nu_0))
  S_1221 = S_1212
  S_2323 = S_1212
  S_2332 = S_1212
  S_3131 = S_1212
  S_3113 = S_1212

elseif (geom == 2)
  % Fiber-like inclusions:
  l = 1000       % fibre length
  d = 1        % fibre diameter
  a = l/d     % aspect ratio
  a2 = power(a,2.0)
  g = (a/power(a2-1,1.5))*(a*sqrt(a2-1)-acosh(a))
  b = 1/(1-nu_0)
```

```
    c = 1-2*nu_0
    e = 1/(a2-1)


    S_1111 = 0.5*b*(c + e*(3*a2-1)-(c+3*e*a2)*g)
    S_2222 = (3/8)*b*e*a2+0.25*b*(c-(9/4)*e)*g;
    S_3333 = S_2222;
    S_2233 = 0.25*b*(0.5*e*a2-(c+0.75*e)*g);
    S_3322 = S_2233;
    S_2211 = -0.5*b*e*a2 + 0.25*b*(3*e*a2-c)*g;
    S_3311 = S_2211;
    S_1122 = -0.5*b*(c+e)+0.5*b*(c+1.5*e)*g;
    S_1133 = S_1122;
    S_2323 = 0.25*b*(0.5*e*a2 + (c-0.75*e)*g);
    S_3232 = S_2323;
    S_1212 = 0.25*b*(c-(a2+1)*e-0.5*(c-3*e*(a2+1))*g);
    S_1313 = S_1212;
    S_3131 = S_1313;


elseif (geom == 3)
    % Disc-shaped inclusions
    l = 0.5        % fibre length
    d = 1        % fibre diameter
    a = l/d     % aspect ratio
    a2 = power(a,2.0)
    g = (a/power(1-a2,1.5))*(acos(a)-a*sqrt(1-a2))
    b = 1/(1-nu_0)
    c = 1-2*nu_0
    e = 1/(a2-1)


    S_1111 = 0.5*b*(c + e*(3*a2-1)-(c+3*e*a2)*g);
    S_2222 = (3/8)*b*e*a2+0.25*b*(c-(9/4)*e)*g;
    S_3333 = S_2222;
    S_2233 = 0.25*b*(0.5*e*a2-(c+0.75*e)*g);
    S_3322 = S_2233;
    S_2211 = -0.5*b*e*a2 + 0.25*b*(3*e*a2-c)*g;
    S_3311 = S_2211;
    S_1122 = -0.5*b*(c+e)+0.5*b*(c+1.5*e)*g;
    S_1133 = S_1122;
    S_2323 = 0.25*b*(0.5*e*a2 + (c-0.75*e)*g);
    S_3232 = S_2323;
    S_1212 = 0.25*b*(c-(a2+1)*e-0.5*(c-3*e*(a2+1))*g);
    S_1313 = S_1212;
    S_3131 = S_1313;
```

```
end

% Eshelby tensor (using engineering strains)
S = zeros(6,6);

% Matrix form:
S(1,1) = S_1111;
S(1,2) = S_1122;
S(1,3) = S_1133;
S(2,1) = S_2211;
S(2,2) = S_2222;
S(2,3) = S_2233;
S(3,1) = S_3311;
S(3,2) = S_3322;
S(3,3) = S_3333;
S(4,4) = 2*S_1212;
S(5,5) = 2*S_2323;
S(6,6) = 2*S_3131;
S;

% Dilute matrix
I = zeros(6,6);
I(1,1) = 1.0;
I(2,2) = 1.0;
I(3,3) = 1.0;
I(4,4) = 1.0;
I(5,5) = 1.0;
I(6,6) = 1.0;
I;

A_dil = inv(I+S*inv(C)*(D-C))
Vf = 0.0:0.001:0.2;

for i =1:length(Vf)
  V0 =(1-Vf(i));
  A_0 = inv(V0*I + Vf(i)*A_dil);
  A_r = A_dil*A_0;
  C_comp = V0*C*A_0 + Vf(i)*D*A_r

  % Calculating the composite elastic stiffness
  if (geom == 1)
    % Isotropic material properties
    nu_c = C_comp(1,2)/(C_comp(1,1)+C_comp(1,2));
```

```
      E_c  = 2*C_comp(4,4)*(1+nu_c);
      E_11(i) = E_c/E_0;
    elseif (geom == 2)
      % Transversely isotropic proerties
      S_comp = inv(C_comp);
      E_11(i) = 1/(S_comp(1,1)*E_0);
    elseif (geom == 3)
      % Transversely isotropic proerties
      S_comp = inv(C_comp);
      E_11(i) = 1/(S_comp(1,1)*E_0);
    end
end


if (geom ==1)
  plot(Vf,E_11,'b')
elseif (geom == 2)
  plot(Vf,E_11,'c')
elseif (geom == 3)
  plot(Vf,E_11, 'r')
end
xlabel ('V_f')
ylabel('E_{comp}/E_m')
```

## B.2  General Mori-Tanaka model for randomly oriented inclusions

```
% Mori-Tanaka – general model
% File name: "mori_tanaka_6.m"
% Generally: Model N-1 shperoidal shaped inclusions in an
% isotropic matrix
% This case: One type of isotropic inclusion
% Three geometries:
% 1) random spherical inclusions
% 2) random fibre-like inclusions with aspect ratio
% 3) random disc-shaped inclusion with aspect ratio
%
% Author: Tom Thorvaldsen, FFI, March 2014

% Elastic parameters - matrix
E_0 = 3.12
nu_0 = 0.35


C = zeros (6,6);
const = (E_0*(1-nu_0))/((1+nu_0)*(1-2*nu_0));
C(1,1) = const;
```

```matlab
C(1,2)= const*(nu_0/(1-nu_0));
C(1,3)= const*(nu_0/(1-nu_0));
C(2,1) = C(1,2);
C(2,2) = const;
C(2,3) = const*(nu_0/(1-nu_0));
C(3,1) = C(1,3);
C(3,2) = C(2,3);
C(3,3) = const;
C(4,4) = const*((1-2*nu_0)/(2*(1-nu_0)));
C(5,5) = const*((1-2*nu_0)/(2*(1-nu_0)));
C(6,6) = const*((1-2*nu_0)/(2*(1-nu_0)));
C;

% Elastic parameters - inclusion
E_i = 386
nu_i = 0.22

D = zeros (6,6);
const = (E_i*(1-nu_i))/((1+nu_i)*(1-2*nu_i));
D(1,1) = const;
D(1,2)= const*(nu_i/(1-nu_i));
D(1,3)= const*(nu_i/(1-nu_i));
D(2,1) = D(1,2);
D(2,2) = const;
D(2,3) = const*(nu_i/(1-nu_i));
D(3,1) = D(1,3);
D(3,2) = D(2,3);
D(3,3) = const;
D(4,4) = const*((1-2*nu_i)/(2*(1-nu_i)));
D(5,5) = const*((1-2*nu_i)/(2*(1-nu_i)));
D(6,6) = const*((1-2*nu_i)/(2*(1-nu_i)));
D;

% Geometry:
geom = 1  % spherical inclusions
%geom = 2  % fibre-like inclusions
%geom = 3  % disc-shaped inclusions

if (geom == 1)
  % Spherical inclusions:
  S_1111 = (7-5*nu_0)/(15*(1-nu_0));
  S_2222 = S_1111
  S_3333 = S_1111
```

```matlab
    S_1122 = (5*nu_0-1)/(15*(1-nu_0));
    S_1133 = S_1122
    S_2211 = S_1122
    S_2233 = S_1122
    S_3311 = S_1122
    S_3322 = S_1122
    S_1212 = (4-5*nu_0)/(15*(1-nu_0))
    S_1221 = S_1212
    S_2323 = S_1212
    S_2332 = S_1212
    S_3131 = S_1212
    S_3113 = S_1212


elseif (geom == 2)
    % Fiber-like inclusions:
    l = 1000      % fibre length
    d = 1         % fibre diameter
    a = l/d       % aspect ratio
    a2 = power(a,2.0)
    g = (a/power(a2-1,1.5))*(a*sqrt(a2-1)-acosh(a))
    b = 1/(1-nu_0)
    c = 1-2*nu_0
    e = 1/(a2-1)

    S_1111 = 0.5*b*(c + e*(3*a2-1)-(c+3*e*a2)*g)
    S_2222 = (3/8)*b*e*a2+0.25*b*(c-(9/4)*e)*g;
    S_3333 = S_2222;
    S_2233 = 0.25*b*(0.5*e*a2-(c+0.75*e)*g);
    S_3322 = S_2233;
    S_2211 = -0.5*b*e*a2 + 0.25*b*(3*e*a2-c)*g;
    S_3311 = S_2211;
    S_1122 = -0.5*b*(c+e)+0.5*b*(c+1.5*e)*g;
    S_1133 = S_1122;
    S_2323 = 0.25*b*(0.5*e*a2 + (c-0.75*e)*g);
    S_3232 = S_2323;
    S_1212 = 0.25*b*(c-(a2+1)*e-0.5*(c-3*e*(a2+1))*g);
    S_1313 = S_1212;
    S_3131 = S_1313;


elseif (geom == 3)
    % Disc-shaped inclusions
    l = 0.00005      % fibre length
    d = 1         % fibre diameter
```

```matlab
  a = l/d      % aspect ratio
  a2 = power(a,2.0)
  g = (a/power(1-a2,1.5))*(acos(a)-a*sqrt(1-a2))
  b = 1/(1-nu_0)
  c = 1-2*nu_0
  e = 1/(a2-1)


  S_1111 = 0.5*b*(c + e*(3*a2-1)-(c+3*e*a2)*g);
  S_2222 = (3/8)*b*e*a2+0.25*b*(c-(9/4)*e)*g;
  S_3333 = S_2222;
  S_2233 = 0.25*b*(0.5*e*a2-(c+0.75*e)*g);
  S_3322 = S_2233;
  S_2211 = -0.5*b*e*a2 + 0.25*b*(3*e*a2-c)*g;
  S_3311 = S_2211;
  S_1122 = -0.5*b*(c+e)+0.5*b*(c+1.5*e)*g;
  S_1133 = S_1122;
  S_2323 = 0.25*b*(0.5*e*a2 + (c-0.75*e)*g);
  S_3232 = S_2323;
  S_1212 = 0.25*b*(c-(a2+1)*e-0.5*(c-3*e*(a2+1))*g);
  S_1313 = S_1212;
  S_3131 = S_1313;
end


% Eshelby tensor (using engineering strains)
S = zeros(6,6);
% Matrix form:
S(1,1) = S_1111;
S(1,2) = S_1122;
S(1,3) = S_1133;
S(2,1) = S_2211;
S(2,2) = S_2222;
S(2,3) = S_2233;
S(3,1) = S_3311;
S(3,2) = S_3322;
S(3,3) = S_3333;
S(4,4) = 2*S_1212;
S(5,5) = 2*S_2323;
S(6,6) = 2*S_3131;
S;


% Dilute matrix
I = zeros(6,6);
I(1,1) = 1.0;
```

```
I(2,2) = 1.0;
I(3,3) = 1.0;
I(4,4) = 1.0;
I(5,5) = 1.0;
I(6,6) = 1.0;
I;


A_dil = inv(I+S*inv(C)*(D-C))


% Averaging matrix
M =(1/120)*[24 64 0 16 16 0 0 0 0 0 0 64;
  24 9 45 6 6 10 10 5 5 20 40 24;
  24 9 45 6 6 10 10 5 5 20 40 24;
  8 8 0 12 32 20 0 40 0 0 0 -32;
  8 8 0 32 12 0 20 0 40 0 0 -32;
  8 8 0 12 32 20 0 40 0 0 0 -32;
  8 8 0 32 12 0 20 0 40 0 0 -32;
  8 3 15 2 2 30 30 15 15 -20 -40 8;
  8 3 15 2 2 30 30 15 15 -20 -40 8;
  8 3 15 2 2 -10 -10 -5 -5 20 40 8;
  8 8 0 -8 -8 0 0 0 0 40 20 28;
  8 8 0 -8 -8 0 0 0 0 40 20 28]


D_A_dil = D*A_dil


% Averaging of D_A_dil
D_A_dil_vec(1) = D_A_dil(1,1);
D_A_dil_vec(2) = D_A_dil(2,2);
D_A_dil_vec(3) = D_A_dil(3,3);
D_A_dil_vec(4) = D_A_dil(1,2);
D_A_dil_vec(5) = D_A_dil(2,1);
D_A_dil_vec(6) = D_A_dil(1,3);
D_A_dil_vec(7) = D_A_dil(3,1);
D_A_dil_vec(8) = D_A_dil(2,3);
D_A_dil_vec(9) = D_A_dil(3,2);
D_A_dil_vec(10) = D_A_dil(4,4);
D_A_dil_vec(11) = D_A_dil(5,5);
D_A_dil_vec(12) = D_A_dil(6,6);


D_A_dil_aver_vec = M*transpose(D_A_dil_vec);


D_A_dil_aver(1,1) = D_A_dil_aver_vec(1);
D_A_dil_aver(2,2) = D_A_dil_aver_vec(2);
```

```
D_A_dil_aver(3,3) = D_A_dil_aver_vec(3);
D_A_dil_aver(1,2) = D_A_dil_aver_vec(4);
D_A_dil_aver(2,1) = D_A_dil_aver_vec(5);
D_A_dil_aver(1,3) = D_A_dil_aver_vec(6);
D_A_dil_aver(3,1) = D_A_dil_aver_vec(7);
D_A_dil_aver(2,3) = D_A_dil_aver_vec(8);
D_A_dil_aver(3,2) = D_A_dil_aver_vec(9);
D_A_dil_aver(4,4) = D_A_dil_aver_vec(10);
D_A_dil_aver(5,5) = D_A_dil_aver_vec(11);
D_A_dil_aver(6,6) = D_A_dil_aver_vec(12);
D_A_dil_aver;


% Averaging of A_dil
A_dil_vec(1) = A_dil(1,1);
A_dil_vec(2) = A_dil(2,2);
A_dil_vec(3) = A_dil(3,3);
A_dil_vec(4) = A_dil(1,2);
A_dil_vec(5) = A_dil(2,1);
A_dil_vec(6) = A_dil(1,3);
A_dil_vec(7) = A_dil(3,1);
A_dil_vec(8) = A_dil(2,3);
A_dil_vec(9) = A_dil(3,2);
A_dil_vec(10) = A_dil(4,4);
A_dil_vec(11) = A_dil(5,5);
A_dil_vec(12) = A_dil(6,6);


A_dil_aver_vec = M*transpose(A_dil_vec);


A_dil_aver(1,1) = A_dil_aver_vec(1);
A_dil_aver(2,2) = A_dil_aver_vec(2);
A_dil_aver(3,3) = A_dil_aver_vec(3);
A_dil_aver(1,2) = A_dil_aver_vec(4);
A_dil_aver(2,1) = A_dil_aver_vec(5);
A_dil_aver(1,3) = A_dil_aver_vec(6);
A_dil_aver(3,1) = A_dil_aver_vec(7);
A_dil_aver(2,3) = A_dil_aver_vec(8);
A_dil_aver(3,2) = A_dil_aver_vec(9);
A_dil_aver(4,4) = A_dil_aver_vec(10);
A_dil_aver(5,5) = A_dil_aver_vec(11);
A_dil_aver(6,6) = A_dil_aver_vec(12);
A_dil_aver;
```

```matlab
Vf = 0.0:0.001:0.2;
for i =1:length(Vf)
  V0 =(1-Vf(i));
  if (geom == 1)
    A_0 = inv(V0*I + Vf(i)*A_dil);    % gives the correct spherical
distr.
  elseif (geom == 2)
    A_0 = inv(V0*I + Vf(i)*A_dil_aver); % gives a transversely iso
C_comp
  elseif (geom == 3)
    A_0 = inv(V0*I + Vf(i)*A_dil_aver);
  end


  C_comp = (V0*C + Vf(i)*D_A_dil_aver)*A_0

  if (geom == 1)
    % Isotropic material properties
    nu_c = C_comp(1,2)/(C_comp(1,1)+C_comp(1,2));
    E_c  = 2*C_comp(4,4)*(1+nu_c);
    E_11(i) = E_c/E_0;
  elseif (geom == 2)
    % Transversely isotropic properties
    S_comp = inv(C_comp);
    E_11(i) = 1/(S_comp(1,1)*E_0);
  elseif (geom == 3)
    % Transversely isotropic proerties%
    S_comp = inv(C_comp);
    E_11(i) = 1/(S_comp(1,1)*E_0);
  end
end

if (geom ==1)
  plot(Vf,E_11,'r')
elseif (geom == 2)
  plot(Vf,E_11, 'c')
elseif (geom == 3)
  plot(Vf,E_11, 'r--')
end
xlabel ('V_f')
ylabel('E_{comp}/E_0')
```

## B.3 Weng model

```
% Refererence: Weng, 1984
% File name: "mori_tanaka_5.m"
% This case: One type of isotropic inclusion
% One geometry: random spherical inclusions
% Author: Tom Thorvaldsen, FFI, March 2014


% Elastic properties - matrix
E_0 = 2.76
nu_0 =  0.35
mu_0 = E_0/(2*(1+nu_0))
kappa_0 = E_0/(3*(1-2*nu_0))


% Elastic properties - inclusion
E_f =  72.4
nu_f = 0.2
mu_f = E_f/(2*(1+nu_f))
kappa_f = E_f/(3*(1-2*nu_f))


V_f = 0.0:0.01:1.0;
for i =1:length(V_f)
  V0 = 1-V_f(i);
  kappa_c(i)=1 + V_f(i)/(((3*V0*kappa_0)/(3*kappa_0+4*mu_0))...
      +(kappa_0/(kappa_f-kappa_0)))
  mu_c(i)= 1+
V_f(i)/((((6/5)*V0*(kappa_0+2*mu_0))/(3*kappa_0+4*mu_0))...
      +(mu_0/(mu_f-mu_0)))

  % Effective Young's modulus (normalized)
  E_c(i)= kappa_c(i)*mu_c(i)*(3*kappa_0+mu_0)/...
      (3*kappa_c(i)*kappa_0+mu_c(i)*mu_0);
end


plot(V_f,E_c, 'g')
xlabel ('V_f')
ylabel('E_{comp}/E_m')
```

## B.4 Qiu and Weng model

```
% Refererence: Qiu and Weng, 1990
% File name: "mori_tanaka_4.m"
%
% This case: One type of inclusion. Includes isotropic and anisotropic
% material properties.
% Three geometries:
% 1) random spherical inclusions
% 2) random needles (circular fibres) inclusions
% 3) random thin discs
%
% Author: Tom Thorvaldsen, FFI, March 2014

% Elastic properties - matrix
E_0 = 3.12
nu_0 =  0.35
mu_0 = E_0/(2*(1+nu_0))
kappa_0 = E_0/(3*(1-2*nu_0))

% Elastic properties - inclusion
E_f =  386
nu_f = 0.22
mu_f = E_f/(2*(1+nu_f))
kappa_f = E_f/(3*(1-2*nu_f))

% Geometry:
geom = 1  % spherical inclusions
% geom = 2  % needles inclusions
%geom = 3  % thin discs

k_1 = kappa_f+(1/3)*mu_f
l_1 = kappa_f-(2/3)*mu_f
n_1 = kappa_f+(4/3)*mu_f
m_1 = mu_f
p_1 = m_1
kappa_1 = (1/9)*(4*k_1+4*l_1+n_1)
mu_1 = (1/3)*(k_1-2*l_1+n_1)

if (geom == 1)
  % Spherical inclusions
  mu_s0 = (mu_0/6)*((9*kappa_0+8*mu_0)/(kappa_0+2*mu_0))
  kappa_s0 =(4/3)*mu_0
  a2_1 = (1/27)*power(n_1+l_1-2*k_1,2.0)
```

```matlab
  V_f = 0.0:0.01:1.0;
  for i =1:length(V_f)
    V0 = 1.0-V_f(i);
    kappa_c(i)=(1/((V0/(kappa_s0+kappa_0))+...
         (V_f(i)/(kappa_s0+kappa_1 -(a2_1/(mu_s0+mu_1))))))-
kappa_s0)/kappa_0;
    mu_c(i)= (1/((V0/(mu_s0+mu_0))+...
         (V_f(i)/5)*((1/(mu_s0+mu_1-(a2_1/(kappa_s0+kappa_1))))+...
         (2/(mu_s0+m_1))+(2/(mu_s0+p_1))))-mu_s0)/mu_0;

    % Effective Young's modulus (normalized)
    E_c(i)= (kappa_c(i)*mu_c(i)*(3*kappa_0+mu_0))/...
         (3*kappa_c(i)*kappa_0+mu_c(i)*mu_0);
  end


elseif (geom == 2)
  % Needles inclusions
  V_f = 0.0:0.01:1.0;
  for i =1:length(V_f)
    V0 = 1.0-V_f(i);
    % Voigt bounds:
    kappa_V = V0*kappa_0+V_f(i)*kappa_1
    mu_V = V0*mu_0+(V_f(i)/5)*(mu_1+2*m_1+2*p_1)
    gamma_0 = (mu_0*(kappa_0+(1/3)*mu_0))/(kappa_0+(7/3)*mu_0)

    kappa_c(i) = (kappa_V...
         -V_f(i)*inv(1-V_f(i)*((2*k_1+l_1-
3*kappa_0)/(3*(k_1+mu_0))))...
         *(((2*k_1+l_1-3*kappa_0)*(2*k_1+l_1-
3*kappa_V))/(9*(k_1+mu_0))))...
         /kappa_0

    mu_c(i) = (mu_V ...
         -(V_f(i)/5)*inv(1-V_f(i)*((k_1-l_1-mu_0)/(15*(k_1+mu_0)))...
         -(2/5)*V_f(i)*((m_1-mu_0)/(m_1+gamma_0))...
         -(2/5)*V_f(i)*((p_1-mu_0)/(p_1+mu_0)))...
         *(((((k_1-l_1-mu_0)*(k_1-l_1-mu_V))/(3*(k_1+mu_0)))...
         +((2*(m_1-mu_0)*(m_1-mu_V))/(m_1+gamma_0))...
         +((2*(p_1-mu_0)*(p_1-mu_V))/(p_1+mu_0))))/mu_0

    % Effective Young's modulus (normalized)
    E_c(i)= (kappa_c(i)*mu_c(i)*(3*kappa_0+mu_0))/...
         (3*kappa_c(i)*kappa_0+mu_c(i)*mu_0);
```

```
    end

elseif (geom == 3)
  % Thin discs
  V_f = 0.0:0.01:0.2;
  for i =1:length(V_f)
    V0 = 1.0-V_f(i);
    % Voigt bounds:
    kappa_V = V0*kappa_0+V_f(i)*kappa_1
    mu_V = V0*mu_0+(V_f(i)/5)*(mu_1+2*m_1+2*p_1)


    kappa_c(i) = (kappa_V...
        -V_f(i)*inv(1-V_f(i)*((2*l_1+n_1-3*kappa_0)/(3*n_1)))...
            *(((n_1+2*l_1-3*kappa_0)*(n_1+2*l_1-
        3*kappa_V))/(9*n_1)))...
        /kappa_0;

    mu_c(i) = (mu_V ...
        -(V_f(i)/5)*inv(1-2*V_f(i)*((n_1-l_1-2*mu_0)/(15*n_1))...
        -(2/5)*V_f(i)*((p_1-mu_0)/(p_1)))...
        *(((((n_1-l_1-2*mu_0)*(n_1-l_1-2*mu_V))/(3*n_1))...
        +((2*(p_1-mu_0)*(p_1-mu_V))/(p_1)))))/mu_0;

    % Effective Young's modulus (normalized)
    E_c(i)= (kappa_c(i)*mu_c(i)*(3*kappa_0+mu_0))/...
        (3*kappa_c(i)*kappa_0+mu_c(i)*mu_0)
  end
end

if (geom ==1)
  plot(V_f,E_c, 'r')
elseif (geom == 2)
  plot(V_f,E_c, 'b')
elseif (geom == 3)
  plot(V_f,E_c, 'k')
end
xlabel ('V_f')
ylabel('E_{comp}/E_m')
```

## B.5  Tandon and Weng

```
% Reference: Tandon and Weng, 1984
% File name: "mori_tanaka_1.m"
% This case: One type of isotropic inclusion
% Three geometries:
% 1) aligned spherical inclusions
% 2) aligned fibre-like inclusions, with a given aspect ratio
% 3) aligned disc-shaped inclusion with aspect ratio
%
% Author: Tom Thorvaldsen, FFI, March 2014


% Elastic properties - matrix
E_0 = 2.76
nu_0 = 0.35
lambda_0 = (E_0*nu_0)/((1+nu_0)*(1-2*nu_0))
mu_0 = E_0/(2*(1+nu_0))


% Elastic properties - inclusion
E_f = 72.4
nu_f = 0.2
lambda_f = (E_f*nu_f)/((1+nu_f)*(1-2*nu_f))
mu_f = E_f/(2*(1+nu_f))


% Constants (independent of the volume fraction of the inclusion)
D_1 = 1+ 2*(mu_f-mu_0)/(lambda_f-lambda_0)
D_2 = (lambda_0+2*mu_0)/(lambda_f-lambda_0)
D_3 = lambda_0/(lambda_f-lambda_0)


% Eshelby tensor (using engineering strains)
S = zeros(6,6);


% Geometry:
geom = 1  % spherical inclusions
%geom = 2  % fibre-like inclusions
%geom = 3  % disc-shaped inclusions


if (geom == 1)
  % Spherical inclusions:
  S_1111 = (7-5*nu_0)/(15*(1-nu_0));
  S_2222 = S_1111
  S_3333 = S_1111
  S_1122 = (5*nu_0-1)/(15*(1-nu_0));
  S_2211 = S_1122
```

```
  S_2233 = S_1122
  S_3311 = S_1122
  S_1212 = (4-5*nu_0)/(15*(1-nu_0))
  S_2323 = S_1212
  S_3131 = S_1212

elseif (geom == 2)
  % Fiber-like inclusions:
  l = 100     % fibre length
  d = 1       % fibre diameter
  a = l/d     % aspect ratio
  a2 = power(a,2.0)
  g = (a/power(a2-1,1.5))*(a*sqrt(a2-1)-acosh(a))
  b = 1/(1-nu_0)
  c = 1-2*nu_0
  e = 1/(a2-1)

  S_1111 = 0.5*b*(c + e*(3*a2-1)-(c+3*e*a2)*g);
  S_2222 = (3/8)*b*e*a2+0.25*b*(c-(9/4)*e)*g;
  S_3333 = S_2222;
  S_2233 = 0.25*b*(0.5*e*a2-(c+0.75*e)*g);
  S_3322 = S_2233;
  S_2211 = -0.5*b*e*a2 + 0.25*b*(3*e*a2-c)*g;
  S_3311 = S_2211;
  S_1122 = -0.5*b*(c+e)+0.5*b*(c+1.5*e)*g;
  S_1133 = S_1122;
  S_2323 = 0.25*b*(0.5*e*a2 + (c-0.75*e)*g);
  S_3232 = S_2323;
  S_1212 = 0.25*b*(c-(a2+1)*e-0.5*(c-3*e*(a2+1))*g);
  S_1313 = S_1212;

elseif (geom == 3)
  % Disc-shaped inclusions
  l = 0.1     % fibre length
  d = 1       % fibre diameter
  a = l/d     % aspect ratio
  a2 = power(a,2.0)
  g = (a/power(1-a2,1.5))*(acos(a)-a*sqrt(1-a2))
  b = 1/(1-nu_0)
  c = 1-2*nu_0
  e = 1/(a2-1)

  S_1111 = 0.5*b*(c + e*(3*a2-1)-(c+3*e*a2)*g);
```

```
    S_2222 = (3/8)*b*e*a2+0.25*b*(c-(9/4)*e)*g;
    S_3333 = S_2222;
    S_2233 = 0.25*b*(0.5*e*a2-(c+0.75*e)*g);
    S_3322 = S_2233;
    S_2211 = -0.5*b*e*a2 + 0.25*b*(3*e*a2-c)*g;
    S_3311 = S_2211;
    S_1122 = -0.5*b*(c+e)+0.5*b*(c+1.5*e)*g;
    S_1133 = S_1122;
    S_2323 = 0.25*b*(0.5*e*a2 + (c-0.75*e)*g);
    S_3232 = S_2323;
    S_1212 = 0.25*b*(c-(a2+1)*e-0.5*(c-3*e*(a2+1))*g);
    S_1313 = S_1212;
end


V_f = 0.0:0.01:1.0;
for i =1:length(V_f)
  % Constants
  B_1 = V_f(i)*D_1 + D_2 + (1-V_f(i))*(D_1*S_1111 + 2*S_2211);
  B_2 = V_f(i)+ D_3 + (1-V_f(i))*(D_1*S_1122 + S_2222 + S_2233);
  B_3 = V_f(i)+ D_3 + (1-V_f(i))*(S_1111 + (1+D_1)*S_2211);
  B_4 = V_f(i)*D_1 + D_2 + (1-V_f(i))*(S_1122+ D_1*S_2222 + S_2233);
  B_5 = V_f(i) + D_3 + (1-V_f(i))*(S_1122 + S_2222 + D_1*S_2233);

  A_1 = D_1*(B_4+B_5)-2*B_2;
  A_2 = (1+D_1)*B_2-(B_4+B_5);
  A = 2*B_2*B_3-B_1*(B_4+B_5);

  % Effective Young's modulus (normalized)
  E_11(i)=A/(A+V_f(i)*(A_1+2*nu_0*A_2))
end


if (geom ==1)
  plot(V_f,E_11)
elseif (geom == 2)
  plot(V_f,E_11,'r')
elseif (geom == 3)
  plot(V_f,E_11, 'k')
end


xlabel ('V_f')
ylabel('E_[22]/E_m')
```

# References

[1] B. H. Cipriano, A. K. Kota, A. L. Gershon, C. J. Laskowski, T. Kashiwagi, H. A. Bruck, and S. R. Raghavan, "Conductivity enhancement of carbon nanotube and nanofiber-based polymer nanocomposites by melt annealing," *Polymer*, vol. 49, no. 22, pp. 4846-4851, 2008.

[2] B. D. Agarwal, L. J. Broutman, and K. Chandrashekhara, *Analysis and performance of fiber composites*, 3rd ed John Wiley&Sons, Inc., 2006.

[3] J. N. Coleman, U. Khan, W. J. Blau, and Y. K. Gun'ko, "Small but strong: A review of the mechanical properties of carbon nanotube-polymer composites," *Carbon*, vol. 44, no. 9, pp. 1624-1652, 2006.

[4] G. M. Odegard, T. C. Clancy, and T. S. Gates, "Modeling of the mechanical properties of nanoparticle/polymer composites," *Polymer*, vol. 46, no. 2, pp. 553-562, 2005.

[5] F. Fisher and L. C. Brinson, "Nanomechanics of nanoreinforced polymers," in *Handbook of theoretical and computational nanotechnology: Functional nanomaterials, nanoparticles, and polymer design*. M. Rieth and W. Schommers, Eds. American Scientific Publishers, 2006, pp. 253-360.

[6] T. Thorvaldsen, "A model study of the effective Young's modulus for randomly distributed short-fiber composites," FFI report 2011/00212 (Ugradert), 2011.

[7] T. Thorvaldsen, B. B. Johnsen, and H. Osnes, "Modelling of nanofibre composites," *Proceedings of the "14th European Conference on Composite Materials"*, 2010.

[8] T. Thorvaldsen, "Modelling the elastic stiffness of nanocomposites using three-phase models," FFI report 2005/00534 (Ugradert), 2015.

[9] T. Thorvaldsen, "Modelling the elastic stiffness of nanocomposites using interphase models," Forsvarets forskningsinstitutt, FFI report 2015/00608, 2015.

[10] J. D. Eshelby, "The determination of the elastic field of an ellipsoidal inclusion, and related problems," *Proceedings of the Royal Society of London*, vol. A241, no. 1226, pp. 376-396, 1957.

[11] J. D. Eshelby, "Elastic inclusions and inhomogeneities," in *Progress in Solid Mechanics,* 2nd ed. I. N. Sneddon and R. Hill, Eds. Amsterdam: North-Holland, 1961, pp. 89-140.

[12] C. Weinberger, W. Cai, and D. Barnett, "Lecture notes - Elasticity of microscopic structures," Standford University,ME340B, 2004.

[13] G. P. Tandon and G. J. Weng, "The effect of aspect ratio of inclusions on the elastic properties of unidirectionally aligned composites," *Polymer Composites*, vol. 5, no. 4, pp. 327-333, 1984.

[14] G. P. Tandon and G. J. Weng, "Average stress in the matrix and effective moduli of randomly oriented composites," *Composites Science and Technology*, vol. 27, no. 2, pp. 111-132, 1986.

[15] T. Mori and K. Tanaka, "Average stress in matrix and average elastic energy of materials with misfitting inclusions," *Acta Metallurgica*, vol. 21, no. 5, pp. 571-574, 1973.

[16]   I. M. Daniel and O. Ishai, *Engineering mechanics of composite materials*, 2nd ed Oxford University Press, Inc., 2006.

[17]   G. J. Weng, "Some elastic properties of reinforced solids, with special reference to isotropic ones containing spherical inclusions," *International Journal of Enginering Science*, vol. 22, no. 7, pp. 845-856, 1984.

[18]   Y. P. Qiu and G. J. Weng, "On the application of Mori-Tanaka's theory involving transversely isotropic spheroidal inclusions," *International Journal of Enginering Science*, vol. 28, no. 11, pp. 1121-1137, 1990.

[19]   B. B. Johnsen, T. R. Frømyr, T. Thorvaldsen, and T. Olsen, "Preparation and characterisation of epoxy/alumina polymer nanocomposites," *Composite Interfaces*, vol. 20, no. 9, pp. 721-740, 2013.

[20]   B. B. Johnsen, A. J. Kinloch, R. D. Mohammed, A. C. Taylor, and S. Sprenger, "Toughening mechanisms of nanoparticle-modified epoxy polymers," *Polymer*, vol. 48, no. 2, pp. 530-541, 2007.

[21]   M. M. Gudarzi and F. Sharif, "Enhancement of dispersion and bonding of graphene-polymer through wet transfer of functionalized graphene oxide," *Polymer Letters*, vol. 6, no. 12, pp. 1017-1031, 2012.

[22]   J. D. Fidelus, E. Wiesel, F. H. Gojny, K. Schulte, and H. D. Wagner, "Thermo-mechanical properties of randomly oriented carbon/epoxy nanocomposites," *Composites: Part A*, vol. 36, no. 11, pp. 1555-1561, 2005.